https://doi.org/10.5194/egusphere-2026-4051
Preprint. Discussion started: 23 September 2026
© Author(s) 2026. CC BY 4.0 License.

Ash Fingers Modify Tephra Sedimentation During a Coarse-Ash-Dominated Eruption: Evidence from the 23 July 2024 Etna Paroxysm

Carolina Díaz-Vecino[1], Jonathan Lemus[1,2], Allan Fries[1], Riccardo Simionato[1,2], Simon Thivet[1,3], Simona Scollo[4], Francesco Amadio[5], Laura Pioli[5], Alexandros Panagiotis Poulidis[6], Valentin Freret-Lorgeril[7] and Costanza Bonadonna[1]

[1] Department of Earth Sciences, University of Geneva, Geneva, 1205, Switzerland.
[2] Department of Computer Science, University of Geneva, Carouge, 1227, Switzerland
[3] Department of Geosciences, University of Fribourg, Fribourg, 1700, Switzerland
[4] Istituto Nazionale di Geofisica e Vulcanologia, Osservatorio Etneo, Piazza Roma 2, 95125 Catania, Italy.
[5] Dipartimento di Scienze Chimiche e Geologiche, Università di Cagliari, Cittadella Universitaria, Monserrato 09042, Italy.
[6] Institute of Environmental Physics, University of Bremen, 28359, Bremen, Germany
[7] Laboratoire Magmas Et Volcans, Université Clermont Auvergne, CNRS, 63000 Clermont-Ferrand, IRD, OPGC, France

Correspondence to: Carolina Diaz-Vecino (carolinadiazvecino@gmail.com)

Abstract. Ash fingers are descending particle-laden plumes that develop beneath volcanic clouds and have been observed during several explosive eruptions worldwide. By promoting collective settling, they modify the atmospheric transport and deposition of volcanic ash and remain a significant source of uncertainty in tephra-dispersal forecasting. However, direct measurements of ash-finger properties are rare, and their depositional signature remains poorly constrained. Here, we investigate ash fingers generated during the 23 July 2024 paroxysmal eruption of Mt. Etna (Italy) using high-resolution visible-wavelength video observations, detailed deposit characterization from ground-based and drone-collected samples, thin-section analyses, disdrometer observations and numerical simulations. The resulting deposit is dominated by coarse ash and shows no evidence of aggregation, providing a unique opportunity to isolate the influence of ash fingers on sedimentation processes. Our observations demonstrate that ash fingers can develop in the absence of abundant fine ash (<63 µm), challenging the commonly held assumption that fine particles are required for their formation. Comparison between observed ash-finger descent velocities and settling velocities calculated for irregular particles indicates that ash fingers were capable of entraining particles up to ~950 µm in diameter. This threshold is highly sensitive to particle shape, highlighting the importance of non-spherical settling behaviour in controlling ash-finger transport. Particle concentration also appears to be a primary control on finger formation, as ash fingers were observed only during phases characterized by high mass eruption rates (MER > 2.5×10^5 kg s^{-1}). Deposit analyses show that ash fingers locally modified proximal sedimentation by increasing the proportion of coarse ash and shifting grain-size distributions toward finer values than expected from individual particle settling. In contrast, simulations of TEPHRA 2, a tephra dispersion model, predict only minor differences between scenarios with and without ash-finger settling. This limited sensitivity could arise because the model assumes spherical particles, leading to an underestimation of the grain-size fraction susceptible to ash-finger entrainment. The discrepancy highlights a fundamental limitation of standard dispersal models based on the assumption of individual settling of spherical particles and suggests that particle morphology must be explicitly considered to realistically represent ash-finger transport and deposition. These findings provide new

constraints on ash-finger dynamics and demonstrate that particle shape exerts a first-order control on the interaction between collective sedimentation processes and tephra deposition, with important implications for volcanic ash forecasting and hazard assessment.

1 Introduction

Ash fingers are descending particle-laden plumes that develop underneath volcanic clouds and, although they have been described under different names such as ash veils, convective instabilities or sediment thermals (Eliasson et al., 2014; Manzella et al., 2015; Freret-Lorgeril et al., 2020). The term ash fingers best captures their defining features and is adopted here. They have been observed to form during several volcanic eruptions worldwide, for instance, Ruapehu volcano in 1996 (Bonadonna et al., 2005b), Soufrière Hills volcano in 1997 (Bonadonna et al., 2002a), Eyjafjallajökull volcano in 2010 (Bonadonna et al., 2011; Manzella et al., 2015), Sakurajima volcano in 2013, 2019 and 2022 (Eliasson et al., 2014; Fries, 2022; Takishita et al., 2024), Stromboli volcano in 2015 (Freret-Lorgeril et al., 2020) and Cumbre Vieja volcano in 2021 (Bonadonna et al., 2023a). The occurrence of ash fingers has important implications for volcanic ash hazards and forecasting (Durant, 2015). By enhancing the downward transport of particles from volcanic clouds, ash fingers can accelerate sedimentation, modify grain-size distributions, and influence the spatial distribution of tephra fallout. Such effects may contribute to discrepancies between observed deposits and predictions based on the independent settling of individual particles. More generally, ash fingers represent one of several processes, alongside particle aggregation (Brown et al., 2012) and turbulence-enhanced sedimentation (Watt et al., 2015), that can affect ash transport and deposition and thereby contribute to uncertainties in ash-dispersion forecasts. Improved understanding of these processes is therefore essential for more reliable assessments of volcanic ash hazards and associated risks.

Although ash fingers have been observed during numerous eruptions, only limited studies are dedicated to understanding their dynamics from field observations due to the difficulty of acquiring suitable observations. Manzella et al., (2015) provided the first quantitative description of ash fingers during the 2010 Eyjafjallajökull eruption, measuring their width, spacing, and descent velocity from high-resolution visible-wavelength videos. Their results yielded finger downward velocities of 1 m s^{-1}, which corresponds to the terminal fall velocity of particles with sizes of 200 µm. However, they found a bimodal grain size distribution (GSD) with both coarse (500 µm) and fine particle (16 µm) modes, showing that ash fingers and aggregation enhanced the premature deposition of fine ash. Following, Fries, (2022) presented a systematic review and measurements of ash finger properties based on visual observations at Mt. Etna, Sabancaya, and Sakurajima volcanoes, mainly quantifying finger widths, spacings, and velocities. That work also provided analytical estimates of maximum particle size entrained in ash fingers and demonstrated that finger width scales with particle volume fraction, resulting in the most comprehensive dataset on finger properties to date.

Regarding the nature and mechanisms of formation of ash fingers, several processes have been proposed to explain them, each acting under different eruptive and atmospheric conditions. The most widely recognized mechanism is the development of

https://doi.org/10.5194/egusphere-2026-4051
Preprint. Discussion started: 23 September 2026
© Author(s) 2026. CC BY 4.0 License.

Settling-Driven Gravitational Instabilities (SDGIs), generated when concentrated suspensions of ash at the base of volcanic clouds become gravitationally unstable. This process has been supported by theoretical analyses, analogue experiments and numerical simulations (Carey, 1997; Hoyal et al., 1999; Carazzo and Jellinek, 2012; Scollo et al., 2017; Fries et al., 2021; Lemus, 2022). Another explanation comes from airborne observations of volcanic plumes at Sakurajima volcano, interpreted with a simplified analytical model as instabilities driven by temperature contrasts between the volcanic plume and the surrounding atmosphere (Eliasson et al., 2014). Wind-induced ash fingers have also been proposed, combining field evidence at Stromboli volcano with qualitative analogue experiments. In this case, counter-rotating rolls generated at the cloud base can trigger ash fingers, showing that such features can also arise in relatively weak plumes with low particle concentration, with their formation being highly sensitive to wind-driven turbulence (Freret-Lorgeril et al., 2020). This is a particular example of how preferential concentration or turbulence-induced clustering (Brandt and Coletti, 2022; Penlou et al., 2023) within volcanic plumes and clouds can generate conditions for the development of ash fingers.

In addition, other phenomena are similar to ash fingers. Among them, mammatus clouds have been observed at the base of volcanic clouds (i.e., Mt. St Helens in 1980) and resemble ash fingers, as they are characterized by the development of descending lobes at the cloud base. However, they are formed due to evaporation or sublimation of ash-hydrometeors, or by cloud-base detrainment, rather than by particle settling alone (Schultz et al., 2006; Durant et al., 2009). Sedimentation Waves (SWs) are classified as another form of collective settling occurring near the vent of sustained eruption columns. Identified through laboratory jet experiments, SWs are described as annular surges of particles and entrained fluid that descend faster than individual fallout, enhancing proximal deposition (Gilchrist and Jellinek, 2021). The diversity of phenomena and interpretations highlights that much remains to be learned about the dynamics of ash fingers and collective particle settling. Direct observations of natural eruptions remain essential to constrain the conditions under which different mechanisms operate. Ash fingers are poorly constrained from post-event analysis of deposits, which can be characterized by bimodal grain size distributions often attributed to eruption where ash aggregation is observed (Manzella et al., 2015; Fries 2022). As a result, the contribution of ash fingers on deposits remains overlooked, despite their potential to significantly accelerate fine ash sedimentation and modify sedimentation patterns. This represents a major limitation for volcanic hazard assessments, since Volcanic Ash Transport and Dispersion Models (VATDMs) assume individual particle settling and do not explicitly account for processes such as ash fingers (e.g., Ash3d, TEPHRA2, FALL3D; Bonadonna et al., 2010; Folch et al., 2009; Schwaiger et al., 2012). Despite recent progress in accounting for collective sedimentation within VATDMs, specifically for aggregation processes (Folch et al., 2010; Egan et al., 2020; Beckett et al., 2022), the influence of ash finger on sedimentation is still not accounted for. Hence, there is a need to integrate ash finger phenomena into modelling frameworks to further refine forecasting capabilities.

To address this gap, this study quantitatively characterizes ash fingers during the 23 July 2024, paroxysmal eruption of Mt. Etna volcano (Italy), for which their development was clearly documented through visible-wavelength video recordings. This eruption provides a rare opportunity to isolate the role of ash fingers, as no evidence of ash aggregation was observed, and the deposit is strongly coarse-dominated. This is particularly significant because previous studies have identified the presence of

https://doi.org/10.5194/egusphere-2026-4051
Preprint. Discussion started: 23 September 2026
© Author(s) 2026. CC BY 4.0 License.

fine ash (<125 µm in water) as a primary control on ash finger formation (Carey, 1997; Carazzo and Jellinek, 2012; Manzella et al., 2015; Scollo et al., 2017; Fries et al., 2021, 2024). In this work, we combine image analysis with detailed deposit characterization to link plume observations to depositional signatures, which allows us to assess the grain-size range affected by ash fingers. In addition, we refine the maximum entrainable particle size by accounting for particle shape in settling velocity calculations and evaluate the role of Mass Eruption Rate (MER) in controlling finger occurrence. Finally, we implement a modified version of TEPHRA2 (Bonadonna et al., 2005b; Connor and Connor, 2006) that incorporates enhanced settling associated with ash fingers. This study provides a first field-based benchmark for representing finger-driven sedimentation and highlighting key limitations of current advection-diffusion frameworks.

1.1 Regional setting

Mt. Etna volcano is located on the eastern side of Sicily (Italy), and it is a stratovolcano with several open-conduit craters, including Bocca Nuova (BN), Voragine (VOR), North East (NEC) and the South East crater (SEC) (Corsaro et al., 2017). Etna volcano exhibits a wide variety of eruptive styles, ranging from Strombolian activity and periodic lava fountain episodes associated with lava flows, as well as tephra plumes that can reach up to 15 km above sea level (a.s.l) (Branca and Del Carlo, 2005; Scollo et al. 2009). In recent decades, explosive activity has intensified with frequent paroxysmal eruptions occurring typically at the SEC and VOR craters (Behncke et al., 2014; Giuffrida et al., 2023; Calvari and Nunnari, 2024). These paroxysms, often clustered in episodic sequences, are characterized by powerful lava fountains that can last a few hours and feed tephra plumes rising up several kilometres above the vent and ash clouds spreading tens to hundreds of kilometres from the source (Calvari et al., 2018; Scollo et al., 2019; Andronico et al., 2021).

Between July-August 2024, Etna volcano experienced a renewed phase of intense paroxysmal activity originating from the VOR crater. After several months of relative quiescence, Strombolian activity resumed in mid-June 2024 and progressively intensified, resulting in a sequence of six lava fountaining episodes between 4 July and 15 August 2024 (Calvari and Nunnari, 2024). These events were characterized by eruptive columns reaching up to 10 kms a.s.l, tephra dispersal over eastern Sicily and repeated lava flows from the western rim of the crater. The 23 July 2024 paroxysm, investigated in this study corresponds to the fourth event of this sequence and produced a sustained volcanic plume accompanied by lava flows and tephra fallout.

Ash fingers have been documented at Mt. Etna volcano on several occasions, including the paroxysmal eruption of 23 November 2013 (Andronico et al., 2015; Scollo et al., 2017), the events of 12 April, 2012 and 3 April, 2013 (Fries, 2022), and more recently the 7 March, 2021 eruption (Thomaidis et al., 2021). While most of these studies report on the presence of ash fingers, they provide little quantitative analysis. Fries (2022) offered the first detailed characterization of the phenomenon by quantifying finger spacing, descent velocities, and the atmospheric conditions controlling their development. Despite these observations, a substantial gap remains in our understanding of ash-finger occurrence at Etna volcano, particularly given the volcano's high frequency of explosive activity and the availability of extensive visual monitoring data. These recurrent explosive events, combined with Etna's accessibility, make it a natural laboratory to investigate plume dynamics and collective sedimentation processes such as ash fingers.

https://doi.org/10.5194/egusphere-2026-4051
Preprint. Discussion started: 23 September 2026
© Author(s) 2026. CC BY 4.0 License.

2 Methodology

2.1 Overview of the campaign

All measurements in this work were conducted in the morning of the 23 July 2024, i.e., during the paroxysmal phase of the eruption, when most tephra emission and dispersion occurred. The observation strategy integrated complementary observational and sampling techniques (Fig. 1; all times reported are in local time, LT = UTC+2). These included: (i) high-resolution visible-wavelength videos of the volcanic plume documenting height evolution, and finger properties throughout the eruption; (ii) drone-based measurements at the L1-site including syn-eruptive tephra sampling and in-situ particle size and concentration measurements using an embedded camera and Optical Particle Counter (OPC); (iii) ground-based syn-eruptive measurements at the L1-site, including tephra collection on adhesive carbon tape mounted on thin section glasses, together with Laser Precipitation Monitor (LPM) disdrometer measurements of particle number, sizes and settling velocities; and (iv) post-eruptive tephra sampling at the C-sites (morning of the 23 July 2024) to determine tephra mass loading and grain-size distributions of the eruption (Fig. 2). Additionally, we obtained information on meteorological conditions on the eruption day (i.e., wind direction and speed) using version 4.0 of the Weather Research and Forecasting (WRF) model (Skamarock et al., 2019) to downscale National Centre for Atmospheric Research (NCAR) Global Forecasting System (GFS) data using 3 one-way domains from 10 km to 1.1 km, progressively focusing over Etna, as part of dedicated forecast support to the campaign.

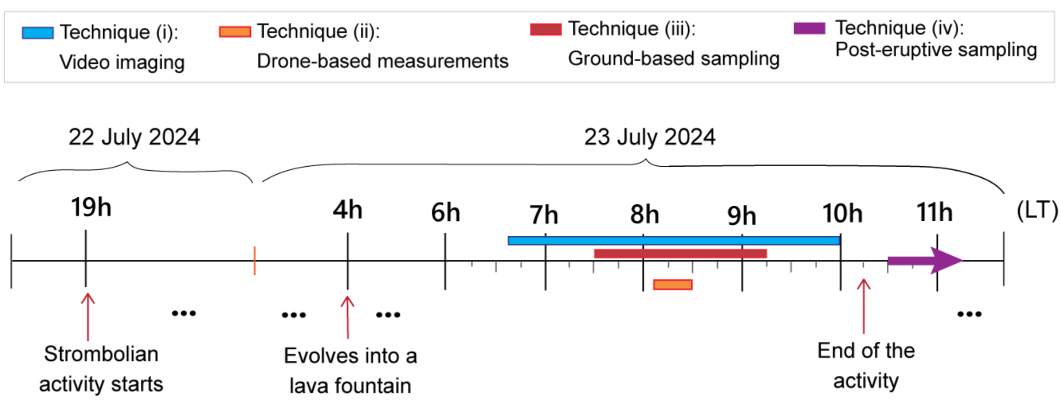

Figure 1: Timeline of the 22-23 July 2024 paroxysmal event of Etna volcano and periods of data acquisition for techniques (i) to (iv). The figure summarizes the progression from the onset of the Strombolian activity at 19:00 LT on 22 July to the development into a sustained lava fountain at approximately 04:08 LT on 23 July, followed by the end of the event at approximately 10:15 LT. Coloured bars indicate the periods during which the different observational techniques were deployed: (i) high-resolution visible-wavelength videos (blue), (ii) drone-based measurements at the L1-site (orange), (iii) ground-based syn-eruptive sampling at the L1-site (red), and (iv) post-eruptive tephra sampling (purple) .Time is shown in local time (LT; UTC+2).

https://doi.org/10.5194/egusphere-2026-4051
Preprint. Discussion started: 23 September 2026
© Author(s) 2026. CC BY 4.0 License.

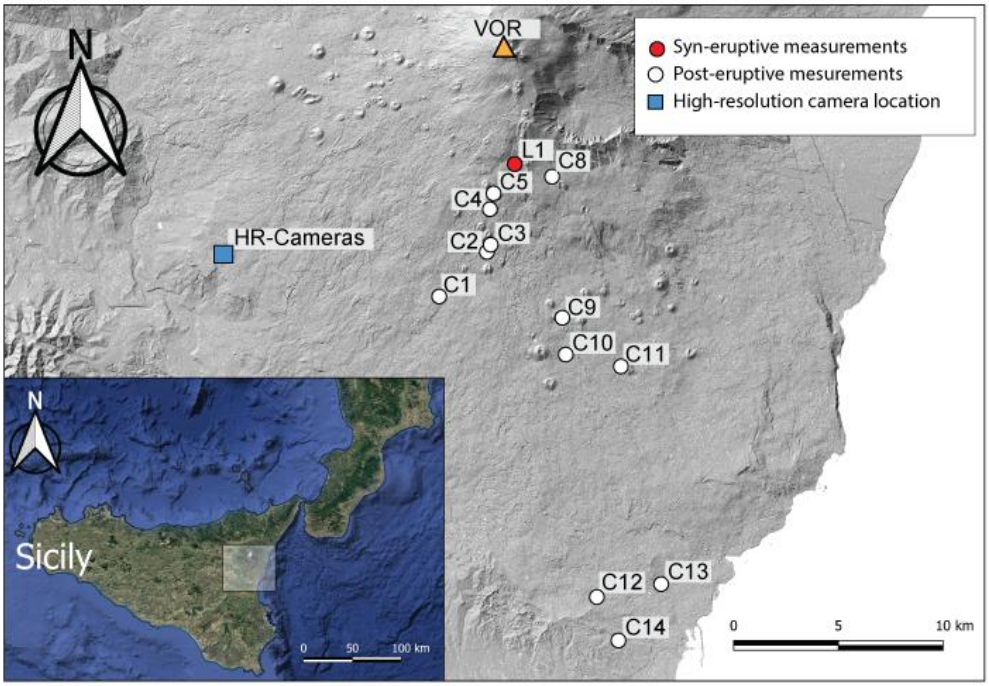

Figure 2: Map of Etna volcano showing the locations of the different data-collection techniques used in this study. The blue square marks the position of the High-Resolution (HR) cameras used for technique (i), which document plume height and finger properties. The red circle indicates the L1-site where technique (ii) drone measurements (syn-eruptive tephra sampling and Optical Particle Counting) and technique (iii) ground-based measurements (disdrometer data and syn-eruptive tephra sampling) were conducted. White circles correspond to the C-sites associated with technique (iv); the post-eruptive tephra sampling carried out on 23 July 2024 morning for grain-size analysis. The orange triangle marks the active crater, Voragine (VOR). Basemap image: Google Earth (31 December 2017)

2.2 High-resolution visible-wavelength videos of the volcanic cloud: video acquisition, image analysis and parameterization

Visible-wavelength videos of the volcanic plume were acquired at a resolution of 1920x1080 pixels and a frame rate of 25 fps (frames per second) using a Nikon D7000 and a Canon Legria HF G40 camera. The cameras were placed in Adrano (37.6612°N, 14.8414°E), approximately 17 km from Etna's summit craters. These recordings were used to determine plume heights between 06:39 and 10:00 LT, and to extract physical parameters of selected ash fingers.

Unfortunately, lighting conditions were not favourable enough to perform the semi-automatic image processing routine available in PlumeTraP (Simionato et al., 2022). Therefore, image analysis consisted of the conversion of the original RGB images to grayscale, followed by a manual contrast adjustment to enhance the visibility of the ash cloud against the background. Then, we exploited the capability of PlumeTraP to apply a geometrical calibration that converts pixel locations into physical coordinates, following also the field of view (FOV) and camera inclination retrievals described in Simionato et al., (2024) and Snee et al., (2023), respectively. The calibration parameters, including camera-image plane distances, horizontal and vertical

https://doi.org/10.5194/egusphere-2026-4051
Preprint. Discussion started: 23 September 2026
© Author(s) 2026. CC BY 4.0 License.

fields of view, camera inclination, and reference geometry are summarized and further explained in Supplementary Fig. S1 and Supplementary Table S1.

Additionally, PlumeTraP incorporates a wind correction following the methodology described in Snee et al., (2023), which accounts for the displacement of the plume by wind. This correction uses wind direction profiles from ERA5 hourly data on pressure levels (Soci et al., 2024) to correct for projection errors in wind-bent plumes, ensuring that retrieved plume measurements are not under or overestimated due to plumes axis not perpendicular to the line of sight of the camera. For all the analyses, systematic uncertainties associated with pixel size and distance from the camera to the vent are automatically quantified during processing.

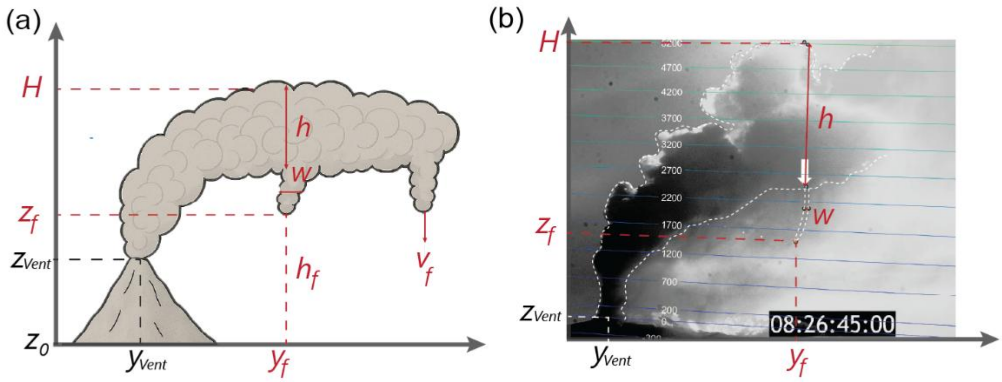

Figure 3: (a) Schematic representation of the plume and finger parameters measured with the PlumeTraP software (parameters highlighted in red), modified from Fries, (2022). (b) Example of a processed video during the peak of the eruption (08:26:45 LT). The plume outline and finger boundaries are shown with white dashed lines, while the measured parameters are indicated in red. Sub-horizontal reference lines correspond to plume height levels corrected for wind displacement distortion. The vent of the volcano is taken as the origin of the coordinate system (z = 0 and y = 0).

This calibration enables the retrieval of key parameters from the ash cloud, including plume height H and cloud thickness h. It also allows for the quantification of finger characteristics such as finger width W, position relative to the vent y_{f}, front height above the vent z_{f}, and downward velocity V_{f} (Fig. 3a. To retrieve these parameters from grayscale images, we used a manual tracking technique (introduced in PlumeTraP from v2.1.0 and further modified for ash fingers measurements in v.2.2.0, Simionato et al., (2024)). Importantly, there are gaps in the plume height record between 08:24 - 08:39 and 08:43 - 08:58 LT, when the plume top rose above the FOV and could no longer be tracked (Fig. 3b). Although a plume height H is traced in Fig. 3b, it is clear that the plume exits the FOV on the right side of the image, indicating that the actual height was greater than what is observed in the image. Nevertheless, during these intervals, ash fingers remained within the FOV and could still be observed and quantified.

2.2.1 Mass Eruption Rate (MER) from plume height measurements

The mass eruption rate (MER) was estimated from plume-height measurements using the analytical model of Degruyter and Bonadonna, (2012), which relates the eruption column height to the source mass flux while accounting for atmospheric

https://doi.org/10.5194/egusphere-2026-4051
Preprint. Discussion started: 23 September 2026
© Author(s) 2026. CC BY 4.0 License.

stratification and wind effects. The model calculates MER as a function of plume height above the vent, atmospheric density, buoyancy frequency and the average wind speed across the plume height. Atmospheric conditions were represented using a standard temperature profile (Woods, 1988), from which the buoyancy frequency was derived. Constant entrainment coefficients of $\alpha = 0.1$ and $\beta = 0.5$, corresponding to the radial and wind entrainment, respectively, were adopted. The MER was calculated for each plume height measurement obtained from the video analysis.

2.3 Ground-based sampling

2.3.1 Adhesive tape sampling

Ash was sampled using the approach of Bagheri et al., (2016) and Diaz-Vecino et al., (2022) by placing a thin section of glass covered with adhesive tape located on the floor, near the LPM. The adhesive tapes were carefully placed in a place shielded from resuspended ash and dust carried by the wind and tephra was collected between 08:10 and 08:18 LT at L1 sampling site. The sample was analysed with a Keyence^{TM} VHX-700 optical digital microscope, which enables high-resolution imaging for quantitative particle analysis. GSDs were reconstructed from the images by applying image binarization techniques and assuming a spherical equivalent diameter for each particle.

2.3.2 Syn-eruptive measurements using a Laser Precipitation Monitor (LPM) optical disdrometer

Real-time measurements of particle size and settling velocities were obtained using a Laser Precipitation Monitor (LPM), a laser-based optical disdrometer developed by Thies Clima^{TM}. This optical disdrometer uses a laser sheet (here 785 nm in wavelength and 46.5 cm^2 in surface) to detect particles settling across the beam. The fall velocity is inferred from the crossing time of each detected particle and the size is retrieved from induced extinction of the laser. Originally designed for meteorological applications, the LPM has more recently been adapted for volcanology to track tephra sedimentation during ongoing eruptions and is capable of detecting particles between 0.15 up to 8.00 mm with fall velocities ranging from 0 to 10 m s^{-1} (Freret-Lorgeril et al., 2022; Bonadonna et al., 2023). In this study, the LPM was deployed at location L1 which is placed at 6 km from the vent (i.e., red point in Fig. 2), and installed approximately 1 m above the ground.

Importantly, Freret-Lorgeril et al., (2022) showed that although LPMs were originally developed for meteorological purposes, they can reliably track the dynamics of tephra fallout. However, raw signals often contain false detections due to instrument limitations and the complex morphology of volcanic particles. To ensure accuracy, the acquired data were subsequently filtered following the protocols proposed by Freret-Lorgeril et al., (2022), which remove detections that are not physically plausible (See Supplementary Fig. S2).

https://doi.org/10.5194/egusphere-2026-4051
Preprint. Discussion started: 23 September 2026
© Author(s) 2026. CC BY 4.0 License.

2.4 Drone-based measurements

An Unoccupied Aircraft Vehicle (UAV) DJI™ Matrice 30 was deployed strictly above the L1-site (Fig. 2), and tephra fallout sampling was operated at 500 m above ground level. Tephra fallout was sampled and measured following the methodology in Thivet et al., (2025), and Thivet et al. (2026) using the Airborne Ash Collector and Counter with Camera (A_2C_2) payload device. The A_2C_2 includes a remotely actuated particle sampling module that contains sample holders equipped with a thin section glass coated with conductive carbon tape, ensuring full compatibility with laboratory imaging and particle analysis techniques, and using the same analysis technique as the adhesive tape collected at ground level (see Section 2.3.1). Beyond ash collection, the A_2C_2 integrates an Alphasense™ N3 OPC allowing in-situ measurement of fine ash grain-size distributions (< 40 µm) as well as reconstructed Particulate Matter PM_1, $PM_{2.5}$ and PM_{10} concentrations, which correspond to the concentrations of particles < 1, < 2.5, and < 10 µm, respectively. Finally, this payload device also includes a Raspberry-Pi camera operating at 120 fps that monitors the particle velocity and behaviour during sampling, also ensuring that the particle collection was correctly operated.

2.5 Post-eruptive tephra sampling

Twelve tephra samples (C1–C5 and C8–C14 in Fig. 2) were collected along the dispersal axis immediately after the paroxysmal episode, extending to the most distal location where no visible deposit was observed. Sampling was conducted in undisturbed zones with collection surfaces ranging from 0.09 to 0.31 m^2. The collected material was then oven-dried at 80 °C for 24 h and subsequently weighed in the laboratory to calculate mass load, derive GSDs, and determine key statistical parameters.

The mass load was calculated from the dry weight of each sample and the corresponding sampling area. The resulting data were imported into QGIS to generate the isomass map. Total Erupted Mass (TEM) was estimated using the exponential method (Pyle, 1989; Fierstein and Nathenson, 1992), the power-law method (Bonadonna and Houghton, 2005), and the Weibull distribution method (Bonadonna and Costa, 2012) (Supplementary Table S2).

Samples were hand-sieved at half-phi intervals across the grain-size range from -4 ϕ to 1 ϕ where $\phi = -log_2(d_{\mathrm{mm}})$. Where necessary, ash fractions finer than 1ϕ were analyzed using a laser diffraction particle size analyzer (Malvern® Mastersizer 3000) to derive GSDs and calculate associated statistical parameters, such as median diameter (Md_{ϕ}) and sorting (σϕ; Inman, (1952)).

2.6 Estimation of ash fingers entrainment limits from particle settling velocities

To quantify the effect of ash fingers on particle sedimentation, we estimated the maximum particle diameter $d_{\max}$ that can be incorporated into these structures. Since ash fingers are necessarily composed of particles with settling velocity V_{p} lower than their downward velocity V_{f} (Hoyal et al., 1999; Carazzo and Jellinek, 2012; Jacobs et al., 2015; Manzella et al., 2015; Fries et al., 2024), $d_{\max}$ corresponds to the particle size for which V_{p} ($d_{\max}$) = V_{f}. In other words, $d_{\max}$ represents the largest particle

https://doi.org/10.5194/egusphere-2026-4051
Preprint. Discussion started: 23 September 2026
© Author(s) 2026. CC BY 4.0 License.

diameter that remains dynamically coupled to the finger rather than settling independently. The individual settling velocity is expressed in Eq. (1) as:

$$V_p = \sqrt{\frac{4gd_{\mathrm{p}}(\rho_p-\rho_{\mathrm{a}})}{3\rho_{\mathrm{a}}C_{\mathrm{D}}}} \tag{1}$$

where g = 9.81 m s^{-2} is the gravitational acceleration, ρ_{p} is the particle density, ρ_{a} is the air density, d_{p} is the particle diameter, and C_{D} is the drag coefficient. For non-spherical particles, C_{D} is obtained using empirical correlations. The formulation of Ganser, (1993) expresses C_{D} as a function of the Reynolds number Re and two shape factors, which can be estimated from a single descriptor such as sphericity. Accordingly, C_{D} is given by Eq. (2) as:

$$C_{\mathrm{D}} = \frac{24}{ReK_1}(1+0.1118(ReK_1K_2)^{0.6567}) + \frac{0.4305K_2}{1+\frac{3305}{ReK_1K_2}} \tag{2}$$

here K_1 and K_2 are the Stokes and Newton shape factors, expressed in Eq. (3),(4) as:

$$K_1 = \left(\frac{1}{3}+\frac{2}{3}\varphi^{-1/2}\right)^{-1}, \tag{3}$$

and

$$K_2 = 10^{1.8148(-log\varphi)^{0.5743}}, \tag{4}$$

with φ the particle sphericity. For Etna samples, we adopt a representative value of φ = 0.70 ± 0.1, derived from morphometric analyses of particle shape. These measurements are based on two complementary approaches, microscope imaging of tephra collected on adhesive tape and particle imaging obtained with the Bettersizer S3+ dynamic image analyser instrument. The reported value corresponds to the average of both methods and uncertainty corresponds to the standard deviation of sphericity measurements. Furthermore, Re is defined in Eq. (5) as:

$$Re = \frac{V_{\mathrm{t}}D\rho_{\mathrm{a}}}{\mu_{\mathrm{a}}}, \tag{5}$$

where V_t is the terminal settling velocity, D is the particle diameter, ρ_a = 0.7 kg m^{-3} is the air density at the altitude at which ash fingers are observed to propagate, and μ_a = 1.562 x 10^{-5} Pa s is the air dynamic viscosity. Because both C_D and Re depend on V_t, the terminal velocity must be obtained iteratively. Stokes' law described in Eq. (6) gives the first estimate:

$$V_{\mathrm{s}} = \frac{gD^2(\rho_p-\rho_a)}{18\mu_a}, \tag{6}$$

with g = 9.81 m s^{-1} and ρ_p = 2431 ± 327 kg m^{-3} .The particle density was determined by water pycnometry analysis (Eychenne and Le Pennec, 2012; Freret-Lorgeril et al., 2019) using samples collected at location L1. To better represent the fraction of the deposit most relevant to ash finger dynamics, we adopt a representative density based on the average of particles finer than 710 µm, as these size classes are the most susceptible to entrainment within ash fingers (See Supplementary Table S3). This value is then successively refined by updating Re, computing C_D, and recalculating V_t until convergence.

To compute d_{max} we substitute V_p with V_f in Eq. (1), which yields Eq. (7) as:

$$d_{max} = \frac{3\rho_a C_D {V_f}^2}{4g(\rho_p-\rho_a)} \tag{7}$$

https://doi.org/10.5194/egusphere-2026-4051
Preprint. Discussion started: 23 September 2026
© Author(s) 2026. CC BY 4.0 License.

Following the methodology presented in Manzella et al. (2015) and Fries, (2022), we can also obtain the particle volume fraction (X_p; Eq. (8)) inside ash fingers using the following relationship:

$$X_\mathrm{p} = \frac{2{V_f}^2\rho_\mathrm{a}}{\sqrt{\pi}\delta_f g(\rho_p - \rho_a)} \quad (8)$$

where δ_f represents half of the finger width ($W/2$).

2.7 Numerical modelling of ash dispersal

Tephra accumulation and spatial distribution from 23 July 2024, Etna eruption were estimated using TEPHRA2 (Bonadonna et al., 2005b; Connor and Connor, 2006). This model computes the ground deposit of tephra released at different heights using an analytical solution of the advection-diffusion equation. In this framework, tephra transport is governed by the balance between wind advection, gravitational settling, and turbulent diffusion. In TEPHRA2, the column is discretized in several release steps based on a vertical distribution of particles. It also discretizes the particle size spectrum and explicitly treats particle-size classes independently by applying a size-selective diffusion law. This behaviour is controlled by two key inputs: (i) the fall-time threshold, which limits the time at which particles settle, changing from linear to a power-law diffusion, and (ii) the diffusion coefficient, which regulates lateral spreading during transport. All input parameters used in our simulations are provided in Supplementary Table S3.

To investigate the influence of collective sedimentation processes, we modified the original TEPHRA2 code similarly to what is typically done to describe particle aggregation in advection-diffusion models (e.g. Bonadonna et al., 2002b; Biass et al., 2014). Specifically, we incorporated the measured d_max derived from ash fingers, computed using Eq. (7) with a sphericity of 1, as the model does not account for particle irregularity. Assuming that the whole fraction is collectively entrained inside ash fingers, all particle-size classes with diameters smaller than d_max were forced to settle with the velocities obtained from our finger analysis. This change was effectively implemented inside the function that calculates the fall time of each size class. (Supplementary Fig. S3). It enabled the model to represent the enhanced settling driven by ash fingers and account for their effect on tephra sedimentation, making fine particles fall faster than the theoretically expected for individual fallout.

In both simulations, the standard TEPHRA2 simulation and the modified TEPHRA 2 simulation incorporating ash fingers, the maximum observed plume height was used as the input column height. This height corresponds to the phase of maximum eruptive intensity, as it represents the conditions under which the largest particles were deposited, thereby providing an upper bound on column height for the analysis.

3 Results

3.1 Overview of the eruption

The volcanic activity episode began at 19:20 LT on the 22 July at the VOR crater. Overnight, the Strombolian activity progressively intensified and evolved into sustained lava fountaining at 04:08 LT on the 23 July, accompanied by continuous

https://doi.org/10.5194/egusphere-2026-4051
Preprint. Discussion started: 23 September 2026
© Author(s) 2026. CC BY 4.0 License.

tephra dispersion initially towards the east-southeast (ESE) and later toward the south-southeast (SSE). During the following hours, the lava jets continued and reached several kilometres above the crater (up to 4.5 km; Calvari and Nunnari, 2024), while the eruptive column reached a maximum height of ca. 9 km a.s.l. The activity gradually decreased and ceased around 10:15 LT (INGV, 2024).

The temporal evolution of the plume height above the vent (H^*) is shown in Fig. 4a. Measurements started at 06:39 LT, when the plume height was relatively low (ca.1.8 km above the vent). Over the following hours, the plume height increased overall, although several short-lived fluctuations were observed, notably around 07:03, 07:48, and 08:08 LT. The plume reached its maximum height of approximately 5.8 km above the vent around 08:20 LT. Notably, this phase coincides with the first observation of ash fingers beneath the volcanic cloud (shaded green region in Fig. 4a). After peaking, the plume height decreased progressively, returning to values near 2 km above the vent by ~ 10:00 LT. After this time and until the end of the eruption at 10:15, the volcanic plume was obscured by meteorological clouds.

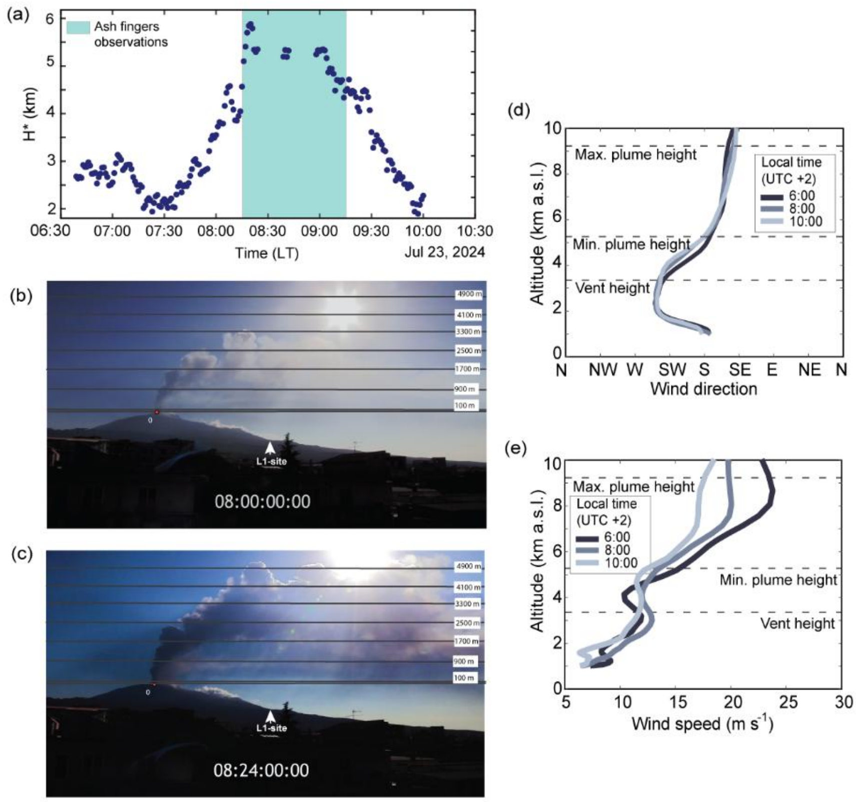

Figure 4: (a) Time series of plume height H^* during the 23 July 2024 Etna eruption derived from visible-wavelength video observations. The shaded area indicates the interval during which ash fingers were visually identified. (b) Visible-wavelength image of the plume at 08:00 LT before the appearance of ash fingers. Horizontal lines indicate altitude above the vent. (c) Visible-wavelength image of the plume at 08:24 LT showing the development of ash fingers during the phase of maximum plume activity. The location of sampling site L1 is indicated. (d) Wind direction profiles derived from the WRF simulations at 06:00, 08:00, and 10:00 LT. Dashed lines indicate vent height, minimum plume height, and maximum plume height. (e) Corresponding wind speed profiles for the same times. Altitudes are expressed in km a.s.l.

https://doi.org/10.5194/egusphere-2026-4051
Preprint. Discussion started: 23 September 2026
© Author(s) 2026. CC BY 4.0 License.

Representative images of the volcanic plume before and during the ash finger development are shown in Fig. 3b-c. At 08:00 LT (Fig. 4b), the plume exhibited no evident ash fingers beneath the cloud. In contrast, by 08:24 (Fig. 4c), ash fingers were clearly visible descending from the base of the volcanic cloud. This image also captures ash fingers depositing directly above sampling location L1 (See Video S1 in the Zenodo repository).

To characterize the atmospheric conditions during the eruption, wind speed and direction profiles derived from the WRF model were analysed for 06:00, 08:00, and 10:00 LT (Fig. 4d-e). The wind direction remained broadly consistent across the three analysed profiles (Fig. 4d). Near the vent level (ca. 3.3 km a.s.l.) and throughout the lower portion of the plume up to ~4 km a.s.l., winds predominantly blew toward the southwest (SW), whereas at higher altitudes the flow shifted toward the southeast (SE). Similarly, wind speed profiles do not show abrupt changes over time (Fig. 4e). Values are relatively weak near the vent altitude, ranging between 10 and 12 m s^{-1}, before undergoing a notable deceleration between 4 and 5 km a.s.l. Above this level, winds accelerate markedly, reaching 18–24 m s^{-1} near the maximum plume height. However, upper-level wind speeds gradually weaken over the course of the eruption, decreasing from ca. 24 m s^{-1} at 06:00 LT to ~18 m s^{-1} at 10:00 LT.

3.2 Ash finger formation and dynamics

Ash fingers were clearly visible during the phase of maximum plume height, between 08:15 and 09:15 LT, coinciding with the most vigorous stage of the eruption. The ash fingers developed at the base of the volcanic cloud, in the transition zone where the convective jet loses vertical momentum and spreads laterally (Fig. 5a). This observation interval corresponds to the period of most intense plume activity, i.e., when the cloud reached heights greater than 5 km above the vent. The visibility of the ash fingers was partly limited by lighting conditions, as the rising sun was positioned directly behind the plume. This reduced the contrast between the ash fingers and their surroundings, preventing continuous and detailed tracking of these structures. Consequently, only two ash fingers could be reliably measured within this time window (Refer to Supplementary Videos S2).

The ash fingers appeared as elongated, downward-moving filaments of a darker tone descending coherently from the base of the cloud. They remained attached to the cloud throughout their evolution and could be tracked downwards as far as the camera's FOV allowed. Fig. 5 illustrates the temporal evolution of Finger 1 at 40 s intervals, showing a clear downward propagation of the finger front as it progressively elongates and becomes more diffuse. The sequence also shows a transition from an initially vertical descent to a slightly backward-bending trajectory in the final frame, which is a general trend when ash fingers reach this altitude (~ 4.8 km a.s.l) during their descent coinciding with the modelled wind shear layer (Fig. 5d).

The mean parameters derived from image analysis of measurable ash fingers are summarized in Table 1. The results show that both ash fingers formed under comparable plume conditions, with mean cloud heights above the finger $\overline{H}$ of 7.2–7.5 km a.s.l. and mean cloud thickness $\overline{h}$ of 1.8–2.1 km. Both ash fingers are characterized by mean widths of approximately 100 m. In contrast, the mean downward velocities differ, with Finger 2 descending more rapidly at 3.6 m s^{-1} compared to 2.5 m s^{-1} for Finger 1.

https://doi.org/10.5194/egusphere-2026-4051
Preprint. Discussion started: 23 September 2026
© Author(s) 2026. CC BY 4.0 License.

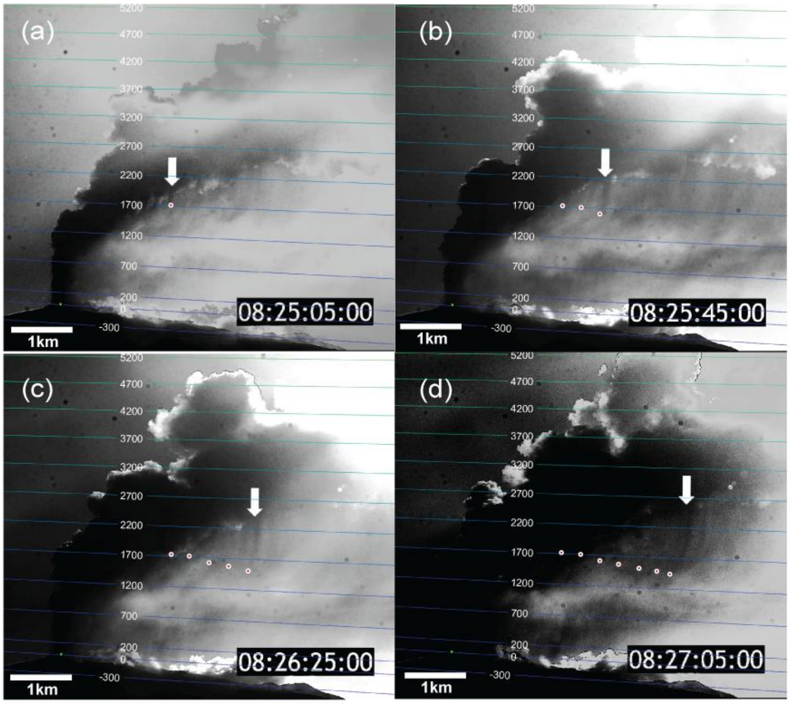

Figure 5: Time sequence for the development of Finger 1, with images shown every 40 s from 08:25:05 to 08:27:05 LT. The white arrow indicates the position of the finger in each frame, and the white points show the evolution of the finger position through time. The image colours were manually adjusted to improve the visibility of the finger. Horizontal lines in the images indicate the altitude above the vent.

Table 1: Measured parameters for each analysed ash finger include the observation time interval, the analysis time step, the mean plume height $\overline{H}$, and the mean plume thickness above the ash finger $\overline{h}$, the mean ash finger front altitude $\overline{z_f}$, the mean finger width $\overline{W}$, and the mean finger downward velocity $\overline{V_f}$. The calculated maximum diameter of irregular particles that can be entrained d_{max-i}, for $\varphi = 0.7 \pm 0.1$ and the particle volume fraction within the ash fingers (X_p) are also listed.

Finger ID	Time interval	Time step (s)	$\overline{H}$ (km a.s.l)	$\overline{h}$ (km)	$\overline{z_f}$ (km a.s.l)	$\overline{W}$ (m)	$\overline{V_f}$ (m s^{-1})	d_{max-i} (µm)	d_{max-i} (ϕ)	X_p
Finger 1	08:25:05-08:27:05	20	7.5 ± 0.6	2.1 ± 0.4	4.7 ± 0.11	100.8 ± 29.8	2.5 ± 0.4	628 ± 144	0.67	4.5×10^{-6}
Finger 2	08:36:02 - 08:37:02	20	7.2 ± 0.2	1.8 ± 0.1	4.8 ± 0.07	98.8 ± 12.2	3.6 ± 0.9	951 ± 236	0.07	1.0×10^{-5}

The d_{max} values calculated from finger velocities and particle characteristics are d_{max-i1} = 628 ± 144 µm (0.67 ϕ) and d_{max-i2} = 951 ± 236 µm (0.07 ϕ), for ash fingers 1 and 2, respectively. As illustrated by the velocity–diameter relationship (Fig. 6), the faster finger (Finger 2; $\overline{V_f}$ = 3.6 m s^{-1}) is capable of transporting coarser particles. Averaging the two measured velocities yields a reference value of d_{max-ia} = 785 ± 190 µm (0.35 ϕ), which is adopted as the reference for the rest of the analysis. These

https://doi.org/10.5194/egusphere-2026-4051
Preprint. Discussion started: 23 September 2026
© Author(s) 2026. CC BY 4.0 License.

estimates further highlight the strong sensitivity of d_{max} to particle shape, because assuming spherical particles (φ = 1) would substantially reduce the maximum particle size that can be entrained within ash fingers, with values ranging from $d_{\mathrm{max-s1}}$= 310 µm (1.7 ϕ) to $d_{\mathrm{max-s2}}$ = 416 µm (1.3 ϕ). Additionally, the corresponding particle volume fractions (X_{p}) range between ~10^{-6} and 10^{-5}, in agreement with the estimation of Manzella et al. (2015).

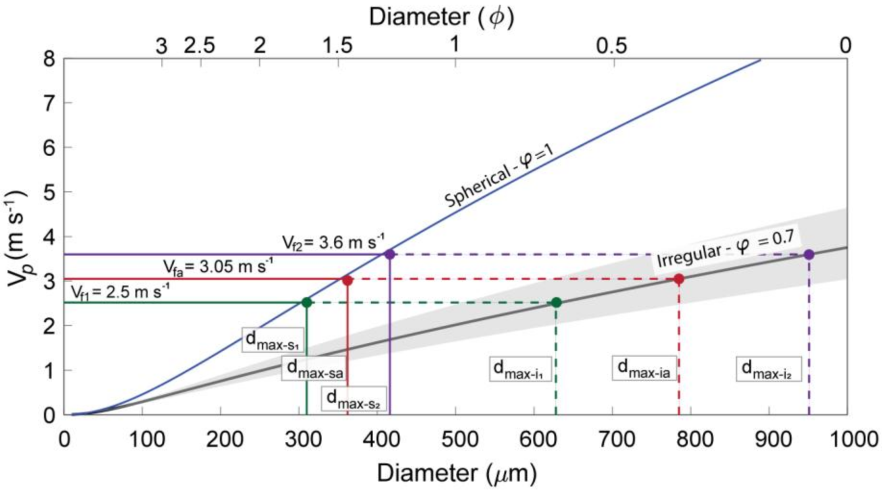

Figure 6: Particle terminal settling velocity (V_{p}) as a function of diameter of particles with different sphericities, including spherical particles (φ =1) and irregular particles (φ = 0.7 ± 0.1; measured from the current eruption samples). The grey shaded area represents the uncertainty associated with the particle shape variability for the irregular case. Horizontal lines indicate the measured downward velocities of the analyzed ash fingers ($\overline{V_{\mathrm{f1}}}$and $\overline{V_{\mathrm{f2}}}$), while V_{fa} denotes the average ash finger descent velocity (V_{fa} = 3.05 m s^{-1}). The intersection between the finger velocities and the particle settling velocity curves define the maximum particles diameter that can be entrained within each finger. Corresponding values are shown for both for spherical ($d_{\mathrm{max-s}}$) and irregular ($d_{\mathrm{max-i}}$) particles.

3.3 Mass Eruption Rate (MER) and its influence on finger occurrence

The Mass Eruption Rate (MER) was estimated using the approach of Degruyter and Bonadonna, (2012), which relies on observed plume height data (Fig. 3a). The MER increased progressively throughout the eruption, although several short-lived fluctuations were observed in the overall increasing trend (Fig. 7). Values remained relatively low during the early stages of the sampling period before rapidly increasing after ca. 07:45 LT and reaching a maximum value of approximately 7.12 × 10^5 kg s^{-1} around 08:20 LT, corresponding to the most vigorous phase of the eruption. Following this peak, the MER declined progressively, returning to values comparable to those at eruption onset by ca. 10:00 LT.

The onset of ash finger development closely coincides with this increase in eruptive intensity. Ash fingers begin to develop once the MER exceeds approximately 2.5 × 10^5 kg s^{-1}, and their occurrence persisted throughout the interval of elevated MER (highlighted in green in Fig. 7). Simultaneously, ground-based LPM measurements collected at the L1-site, located 6 km from the vent, recorded ash sedimentation between 07:33 and 09:16 LT (red line in Fig. 7).

https://doi.org/10.5194/egusphere-2026-4051
Preprint. Discussion started: 23 September 2026
© Author(s) 2026. CC BY 4.0 License.

During the early low-MER phase, the proportion of particles with diameters below $d_{\mathrm{max-ia}}$= 785 µm fluctuated considerably. As the MER intensified, this proportion increased markedly, approaching 100% during the peak activity phase between 08:20 to 08:40 LT. This interval broadly overlaps with the period during which ash fingers were observed beneath the cloud. The light grey shading represents the uncertainty bounds on the $d_{\mathrm{max-ia}}$ threshold. Following the peak activity phase, the proportion of particles below $d_{\mathrm{max-ia}}$ declined progressively, dropping below 70% after 08:55 LT. At 09:16 LT, LPM measurements ceased.

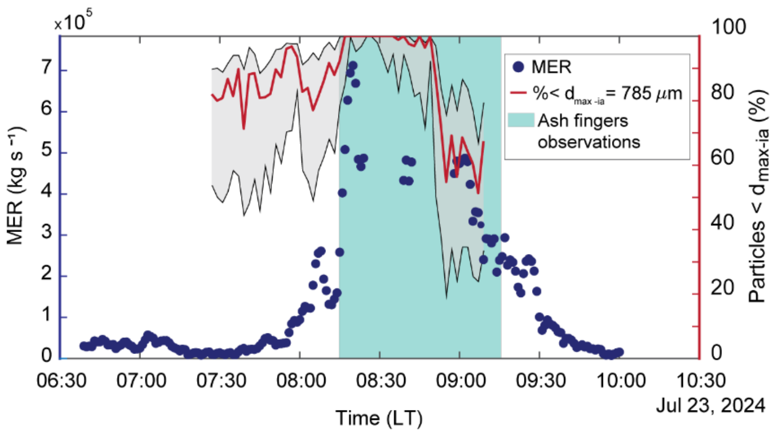

Figure 7: Mass Eruption Rate (MER) estimated from plume height measurements using the methodology of Degruyter and Bonadonna, (2012). Blue markers represent the temporal evolution of MER, while the red curve (right axis) shows the proportion of particles with diameters smaller than $d_{\mathrm{max-ia}}$ = 785 µm measured by the LPM at sampling location L1. The light gray envelope represents the uncertainty associated with the $d_{\mathrm{max-ia}}$ threshold. The green shaded region corresponds to the interval of observed ash fingers.

3.4 Effect of ash fingers on the deposit

The deposit from the 23 July 2024, paroxysmal eruption dispersed southward, with mass load concentrated within the first ca. 12 km from the vent and narrow isomass contours in the proximal region (Fig. 8a). The total grain-size distribution shows a unimodal trend with a dominant mode between 0.5 and 1 ϕ (710–500 µm), a median of Md_{ϕ} = 0.22 ϕ (≈ 860 µm), and a sorting coefficient σ_{ϕ}= 1.04, indicating moderately well-sorted, coarse-to-medium ash fallout (Fig. 8b). The post-eruptive samples span distances of 6.7 – 29.9 km from the vent and record mass loads ranging from 0.08 to 0.083 kg m^{-3} (Table 2), providing a broad spatial coverage of both the proximal and distal portions of the deposit. Based on their spatial distribution relative to the vent and the main sedimentation axis, the collected samples were divided into three groups (Fig. 8a). Group G1 comprises proximal samples located west of the sedimentation axis (C1–C5; Fig. 8c). Group G2 consists of proximal samples situated east of the sedimentation axis (C8–C11; Fig. 8d). Group G3 includes more distal samples collected further downwind to the east (C12–C14; Fig. 8e).

https://doi.org/10.5194/egusphere-2026-4051
Preprint. Discussion started: 23 September 2026
© Author(s) 2026. CC BY 4.0 License.

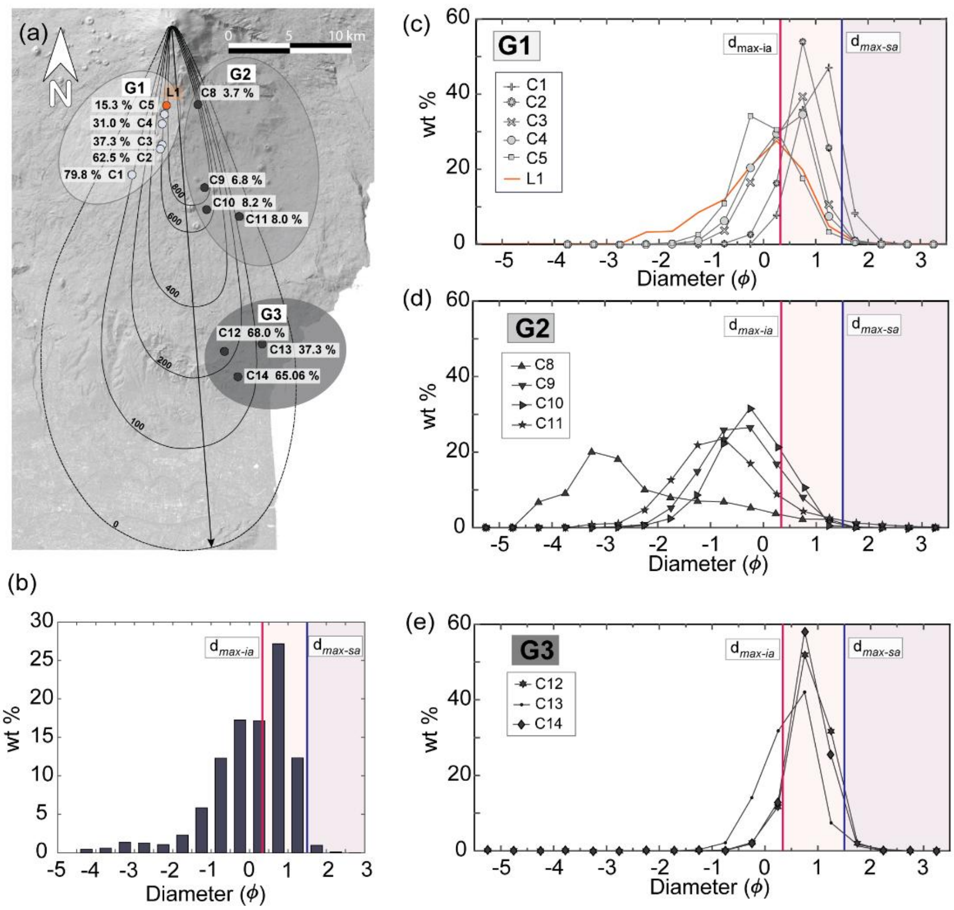

Figure 8: (a) Iso-mass map of the 23 July 2024 Etna eruption, showing mass-load contours (g m^{-2}) where the red point is the L1 Location and the remaining grey-shaded points indicate the C-samples collected for this study and the black arrow shows the predominant sedimentation direction. The shaded ellipses delineate the three sample groups (G1–G3), and the percentages reported beside each sample indicate the proportion of particles finer than d_{max-ia} ($<0.35\ \phi$) (b) Total Grain-size distribution (TGSD) of the whole deposit expressed as weight percent versus particle diameter (ϕ). (c-e) Grain-size distributions (GSDs) for Groups G1, G2 and G3, respectively, expressed as weight percent versus particle diameter (ϕ). The orange grain-size distribution in panel (c) represents sample L1 measured with the LPM from 07:25 to 09:27 LT. The red line marks d_{max-ia} = 0.35ϕ and the blue line marks d_{max-sa} = 1.5ϕ corresponding to the maximum particle diameters susceptible to finger-driven settling derived from d_{max} for the irregular and spherical case, respectively.

Table 2: Characteristics of the post-eruptive tephra samples collected on 23 July 2024, including the group to which they belong, geographic coordinates, distance from the vent (the VOR crater in Fig. 2), elevation, measured tephra mass load, and GS parameters Md_{ϕ} and σ_{ϕ}. Sampling locations were distributed along the main dispersal axis of the deposit (Fig. 8a).

Sample name	Group	Latitude	Longitude	Distance from vent (km)	Elevation (m a.s.l.)	Mass load (kg m^{-2})	GS	
							Md_{ϕ}	σ_{ϕ}

https://doi.org/10.5194/egusphere-2026-4051
Preprint. Discussion started: 23 September 2026
© Author(s) 2026. CC BY 4.0 License.

C1	Group 1	37.6434331	14.9573983	12.50	912	0.09	1.06	0.40
C2		37.6630461	14.9833724	9.95	1162	0.19	0.78	0.40
C3		37.6656112	14.9853687	9.66	1227	0.58	0.51	0.54
C4		37.6808167	14.9852664	7.95	1517	0.40	0.37	0.58
C5		37.6878952	14.9874293	7.14	1660	0.13	0.03	0.56
C8	Group 2	37.6952111	15.0192289	6.73	1697	0.75	-2.62	1.41
C9		37.6339519	15.0242436	13.43	876	0.83	-0.45	0.74
C10		37.6178844	15.0265058	15.22	727	0.60	-0.25	0.65
C11		37.6131329	15.0563751	16.45	603	0.08	-0.81	0.88
C12	Group 3	37.5138037	15.0425708	26.81	143	0.23	0.84	0.38
C13		37.5194516	15.0776323	26.89	61	0.09	0.52	0.47
C14		37.4946963	15.0548386	29.90	83	0.12	0.79	0.35

Group G1, located between 7.1 and 12 km from the vent, shows variability in grain-size distribution together with a progressive fining trend with distance. The most proximal sample (C5) is characterized by a mode between −0.5 and 0 ϕ. Samples C4 to C2 show a shift toward finer material, with modes between 0.5 and 1 ϕ. In contrast, the most distal sample in this group exhibits a finer mode between 1 and 1.5 ϕ. Independent measurements from the LPM in sampling site L1, which sampled tephra fallout between 07:25 to 09:27 LT, yield a median grain size of 0.04 ϕ and a dominant mode between 0 and 0.5 ϕ. The GSD similarity between L1 and Group G1 provides independent support that the G1 deposits formed as a result of the paroxysmal activity. In comparison, Group G2, located between 6.7 and 16.4 km from the vent, exhibits a distinctly different grain-size behaviour. The most proximal sample (C8) is dominated by a very coarse mode between −3.5 and −3 ϕ, indicating a strong contribution from coarse lapilli-sized material. Moving downwind, sample C9 shows a clear shift toward finer fractions, with a dominant mode between −1 and −0.5 ϕ. Samples C10 and C11 display a further transition, with modes centered between −0.5 and 0 ϕ. These modal values are comparable to those observed in sample C5, the western group's most proximal sample. Further east and downwind, Group G3 (C12-C14) show consistently finer grain size distributions, with dominant modes between 0.5 and 1, similar to those observed in the finer samples of Group G1 (C2–C4).

To assess the potential contribution of finger-driven sedimentation to the deposit, we examined the proportion of mass falling below the maximum particle diameter susceptible to finger entrainment. This threshold was defined for irregular and spherical particles as $d_{\mathrm{max-ia}}$= 0.35ϕ (785 µm) and $d_{\mathrm{max-sa}}$=1.5 ϕ (355 µm), respectively (Fig. 6). We also calculated the median grain size (Md_{ϕ}) for each sample as a function of distance from the vent (Fig. 9). The spatial distribution of particles smaller than $d_{\mathrm{max-ia}}$ reveals two distinct groups with elevated finger-susceptible mass fractions. The Group G1 exhibits values greater than 50%, while Group G3 shows comparable proportions exceeding 60%. In contrast, Group G2 displays markedly lower values, remaining below 20%. A general correspondence is observed between finer Md_{ϕ} values and higher proportions of particles smaller than $d_{\mathrm{max-ia}}$, suggesting a direct relationship between overall grain size and the mass fraction susceptible to finger entrainment.

https://doi.org/10.5194/egusphere-2026-4051
Preprint. Discussion started: 23 September 2026
© Author(s) 2026. CC BY 4.0 License.

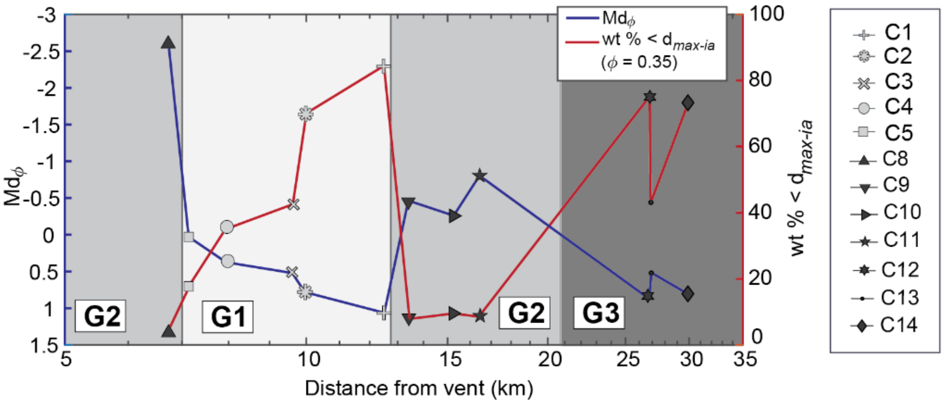

Figure 9: Median grain size (Md_ϕ, solid blue line) and weight percentage below d_{max-ia} (ϕ = 0.35, 785 µm; solid red line) as a function of distance from the vent for all collection sites (C1-C14). Shaded regions indicate the three sample groups (G1, G2, and G3).

3.5 Absence of ash aggregation

To further investigate whether ash aggregation occurred throughout the eruption, we combined optical microscopy of drone and ground collected samples with *in-situ* PM concentration measurements 500 m above the L1-site. (Fig. 2Error! Reference source not found.) during the 08:10-08:17 LT sampling interval (Fig. 10Error! Reference source not found.). Optical microscopy images of the drone sample (Fig. 10a-b) show irregularly shaped particles with no evidence of clustering or aggregation. Image-based grain-size analysis **(**Fig. 10c) indicates a distribution dominated by intermediate-sized ash, with most particles concentrated between 0 and 1 ϕ (500 µm to 1 mm). Similarly, the ground-collected sample (Fig. 10Error! Reference source not found.d-e) consists predominantly of individual particles, with no evidence of aggregation, and contains a larger number of particles than the drone sample. Its grain-size analysis (Fig. 10f) shows the same modal range between 0 and 1 ϕ.

The time series of particulate matter concentrations measured by the OPC shows the PM_1, $PM_{2.5}$, and PM_{10} concentrations (Fig. 10g). During the 23-minute-long measurement interval (08:07 to 08:30 LT), the three fractions exhibit similar temporal behaviour, with no pronounced spikes or abrupt changes; their values are comparable to baseline levels in the atmosphere. In particular, PM_{10} concentrations remain below 30 µg m^{-3} throughout the flight. These results agree with the grain-size data, which show that ash particles smaller than 10 µm are absent, and that no fine particles are evidenced to play a role in ash aggregation. In contrast to the November 11, 2023, in the Sakurajima case described by Thivet et al., (2025) elevated fine-particle concentrations and widespread particle aggregation were observed.

https://doi.org/10.5194/egusphere-2026-4051
Preprint. Discussion started: 23 September 2026
© Author(s) 2026. CC BY 4.0 License.

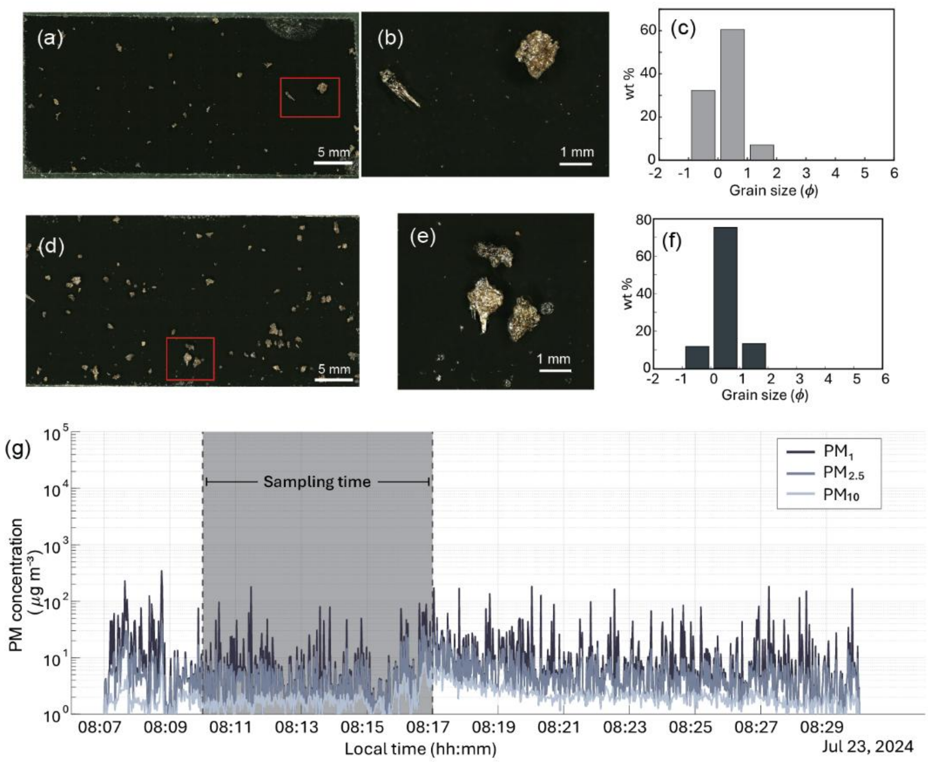

Figure 10: (a) Optical microscopy image of the ash collected by the drone at L1-site during the 08:10–08:17 LT sampling interval (full-scale view). (b) Close-up of the area highlighted by the red box in (a). (c) Grain-size distribution (wt %) obtained from image analysis of the drone-collected sample. (d) Optical microscopy image of the ash collected on the ground at L1-site during the same 08:10–08:17 LT interval (full-scale view). (e) Close-up of the region marked in (d). (f) Grain-size distribution (wt %) derived from image analysis of the ground-collected sample. (g) Time series of particulate matter concentrations (PM_1, $PM_{2.5}$, and PM_{10}) measured by the OPC. The shaded window indicates the sampling period for both drone and ground collections.

3.6 Effect of finger-driven sedimentation on simulated tephra dispersal

To help isolate the effect of finger-driven sedimentation on tephra dispersal under simplified conditions, we ran two TEPHRA2 simulations, i.e., a standard run and a modified run to describe finger-driven sedimentation. In the latter, particles smaller than $d_{\mathrm{max-sa}}$ were assigned a fixed terminal fall velocity of 3.0 m s^{-1}, corresponding to the average measured ash finger descent velocity (V_{fa}) (Fig. 5). As TEPHRA2 does not account for particle shape, the spherical threshold $d_{\mathrm{max-sa}} = 1.5\phi$ (355 μm) was adopted for the modified simulation.

The isomass maps produced by the two simulations are broadly similar (Fig. 11a-b), with the dispersal pattern and contour geometry remaining largely unchanged. The only notable difference occurs at the outermost isomass contour (0.1 kg m^{-2}), which extends farther southward in the standard simulation and includes the distal sample C13 from Group G3, whereas in the

https://doi.org/10.5194/egusphere-2026-4051
Preprint. Discussion started: 23 September 2026
© Author(s) 2026. CC BY 4.0 License.

modified simulation C13 falls outside the predicted deposit extent.. The remaining distal samples from Group G3 (i.e., C12 and C14) remain outside the 0.1 kg m^{-2} contour in both simulations.

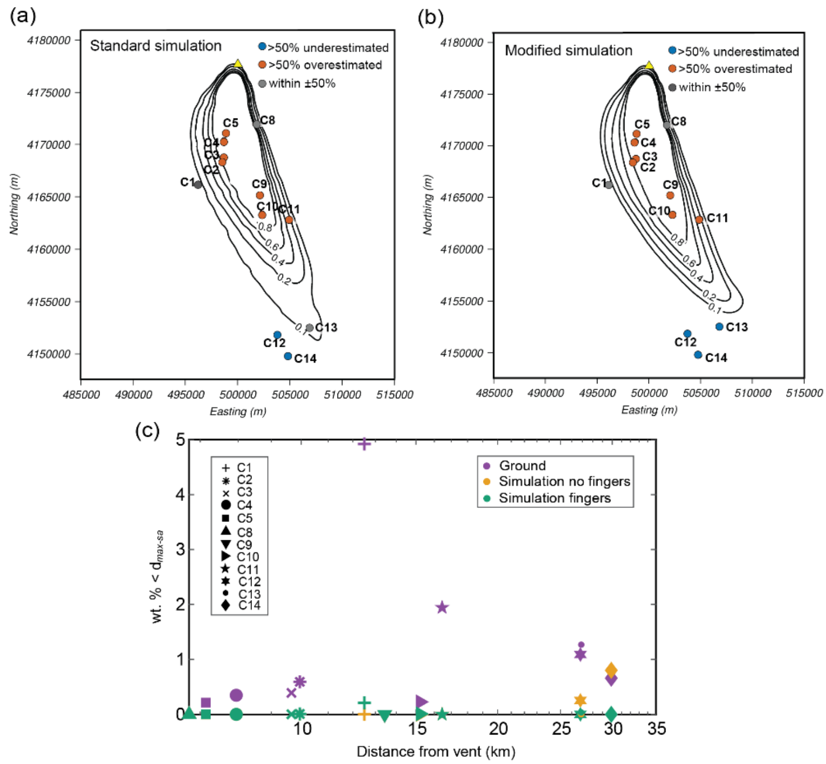

Figure 11: Isomass maps (kg m⁻²) for the baseline (a) and finger-modified (b) simulations. In the baseline simulation, all particle-size classes settle according to standard advection–diffusion dynamics without finger-driven enhancement. In the finger-modified simulation, all particle-size classes finer than $d_{\mathrm{max-sa}}$= 1.5ϕ are assigned an enhanced settling velocity of 3.05 m s⁻¹. The yellow triangle denotes the vent location at Mt. Etna, and labelled circles indicate the collection sites (C1–C14). Point colours indicate model performance relative to the observed mass accumulation at each sampling site: red symbols denote sites where the deposit is overestimated by more than 50%, blue symbols denote sites where the deposit is underestimated by more than 50%, and grey symbols indicate agreement within ± 50% of the observations. (c) Mass fraction (wt%) of particles finer than $d_{\mathrm{max-sa}}$ as a function of distance from the vent for ground measurements (purple), the baseline simulation (yellow), and the finger-modified simulation (green).

The spatial distribution of agreement between simulated and observed mass loading is also similar between the two simulations (Fig. 11a-b). In both cases, the simulated mass loading exceeds the mass loading measured at several proximal sampling locations, particularly at samples C2 -C5 from group G1 and samples C9-C11 from Group G2, resulting in mass overestimations greater than 50%. In contrast, the simulated mass loading at distal sites C12 and C14 from Group G3 is more than 50 % lower than the corresponding measured values in both simulations. The modified simulation further underestimates the mass loading at sample C13, which is reproduced within the ± 50% of the observations in the standard simulation. Only a limited subset of proximal sites, including C1 and C8 is reproduced within the ± 50% of the mass loading measured at in the ground.

https://doi.org/10.5194/egusphere-2026-4051
Preprint. Discussion started: 23 September 2026
© Author(s) 2026. CC BY 4.0 License.

Despite imposing enhanced settling velocities for particles finer than d_{max-sa}, the modified simulation produces only minor changes in the overall deposition pattern and does not substantially increase proximal mass accumulation relative to the standard simulation. Similarly, the proportion of deposited particles finer than d_{max-sa} remains very small in both simulation and differ only slightly between them (Fig. 11c). These results indicate that, using a spherical representation of particle settling, only a small fraction of the deposited mass is affected by finger-driven settling, resulting in minimal changes to the modified deposit (Fig. 11b). This behaviour contrast with the observations, which show larger proportions of particles finer than 1.5 ϕ in several deposit samples (Fig. 11c).

4 Discussion

4.1 Physical controls on ash-finger formation

Observations from the 23 July 2024, paroxysmal eruption of Etna provides new constraints on the dynamics of ash fingers. Previous studies have identified two primary controls on finger formation: the presence of fine ash and high MER that reflects in high particle concentrations. Eruptions in which ash fingers have been documented typically contain a substantial fraction of fine particles, including the 2010 eruption of Eyjafjallajökull (Manzella et al., 2015), the 1996 eruption of Mt. Ruapehu (Bonadonna et al., 2005b), and the 2019 eruptions of Sakurajima (Fries, 2022). Consistent with these observations, laboratory experiments have shown that settling-driven gravitational instabilities develop preferentially when fine particles are abundant (Carey, 1997; Carazzo and Jellinek, 2012; Manzella et al., 2015; Scollo et al., 2017; Fries et al., 2021, 2024). In contrast, the present eruption is strongly coarse-dominated, with a median grain size of Md_{ϕ} = 0.22 ϕ (~860 µm) and a negligible proportion of fine ash particles (Fig 8b). Despite the scarcity of fine ash, well-developed ash fingers were observed beneath the cloud (Fig. 4c). Therefore, this eruption represents one of the few documented coarse-dominated events in which ash fingers have been reported, along with the April 2012, April 2013 and November 2013 eruptions of Mt. Etna volcano, highlighting that all currently documented coarse-dominated cases have been observed at Mt. Etna volcano (Andronico et al., 2015; Fries, 2022). Importantly, the present study provides the first multidisciplinary investigation of how ash fingers influence particle dispersal in coarse-dominated eruptions.

Particle concentration represents a second key control on finger formation (Scollo et al., 2017; Fries et al., 2021, 2024). During the eruption, the appearance of ash fingers beneath the cloud between 08:15 and 09:15 LT coincided with a period of relatively high MER (i.e., 2×10^5 kg s^{-1} < MER < 7×10^5 kg s^{-1}; Fig. 7). Laboratory experiments by Scollo et al. (2017) demonstrate that the formation of gravitational instabilities is fundamentally controlled by particle concentration, with a critical threshold below which ash fingers cannot develop. Because particle concentration in the plume scales with MER, they proposed that only eruptions exceeding 10^5 kg s^{-1} are likely to generate ash fingers. This interpretation is supported by multiple natural examples including Eyjafjallajökull and Ruapehu, all characterized by MER on the order of 10^5 kg s^{-1}, whereas lower-intensity eruptions (~10^4 kg s^{-1}) did not produce observable ash fingers. However, this threshold should be interpreted as a proxy for a

https://doi.org/10.5194/egusphere-2026-4051
Preprint. Discussion started: 23 September 2026
© Author(s) 2026. CC BY 4.0 License.

critical particle concentration rather than a fixed eruptive condition. Recent observations indicated that ash fingers may form below relatively weak plumes, such as the ones at Sakurajima volcano (Takishita et al., 2024) and Stromboli volcano (Freret-Lorgeril et al., 2020), suggesting that the onset of the instability depends on the combined effects of particle loading, plume dynamics and atmospheric structure. In this context, the high MER values observed during the 23 July 2024, eruption likely persisted for sustained particle concentrations well above the critical threshold, promoting ash fingers for an extended time interval (~ 1h).

Additionally, ambient wind may have contributed to the spatial organization of the instability. Freret-Lorgeril et al., (2020) proposed that when the characteristic timescale for wind-driven organization of the plume ($t_{\mathrm{w}} = h\ /v_{\mathrm{w}}$) becomes comparable to the particle settling timescale, counter-rotating rolls may develop within the ash cloud, locally enhancing particle concentration at the cloud base and promoting gravitational instabilities. Here, h represents the characteristic width of the cloud at the altitude where fingers first became visible, whereas v_{w} corresponds to the ambient horizontal wind speed derived from WRF simulations. Using the observations from the 23 July 2024 eruption at 08:24 LT, plume dimensions (h ≈ 1.3 × 10^3 m) and wind speed during the finger-forming phase (v_{w} = 16 ± 5 m s^{-1}; Fig. 4e**)**, we estimate a wind-organization timescale of t_w ≈ 86 ± 27 s. If wind-driven organization contributed to finger formation, the distance at which fingers first appear is expected to be of the same order as the cloud thickness. Consistent with this expectation, the closest ash finger was observed at a distance of ~ 1.6 × 10^3 m from the source, which is comparable to the estimated cloud thickness (See Supplementary Fig. S4). This similarity suggests that wind-driven rolls may have had sufficient time to concentrate particles within the PBL before finger onset, promoting the development of gravitational instabilities.

4.2 A revised definition of d_{max} based on irregular particle shape

A key outcome of this study is the refinement of the maximum particle size that can be entrained by ash fingers (d_{max}), based on the dynamic balance between particle settling velocity and finger downward velocity. In this framework, d_{max} is defined as the particle diameter for which the individual settling velocity equals the downward velocity of the finger ($V_p(d_{\mathrm{max}}) = V_{\mathrm{f}}$), such that particles with $V_{\mathrm{p}} < V_{\mathrm{f}}$ remain coupled to the descending structure, whereas coarser particles decouple and settle independently. Unlike previous approaches that rely on simplified or spherical assumptions (i.e., Fries, 2022) , this formulation incorporated the dependence of settling velocity on particle shape through the drag coefficient (C_{D}). This demonstrates that particle shape exerts a first-order control on d_{max}. For a calculated sphericity of φ = 0.7 ± 0.1, representative of this eruption at Etna, the reduced aerodynamic efficiency of irregular particles leads to lower velocities for a given diameter. Hence, larger particles can be transported within ash fingers, yielding $d_{\mathrm{max-i2}}$ values up to 951 μm for the fastest observed finger ($\overline{V_{\mathrm{f2}}}$= 3.6 m s^{-1}). In contrast, assuming spherical particles (φ = 1) reduces the drag coefficient and, therefore, increases settling velocities, restricting the maximum entrainable size to significantly smaller values, such as $d_{\mathrm{max-s2}}$= 416 μm (Fig. 6).

https://doi.org/10.5194/egusphere-2026-4051
Preprint. Discussion started: 23 September 2026
© Author(s) 2026. CC BY 4.0 License.

Importantly, this formulation highlights that particle shape strongly controls settling behaviour, such that irregular particles experience greater drag and, therefore, lower settling velocities for a given diameter (Bagheri and Bonadonna, 2016b; Saxby et al., 2018, 2020). As a consequence, significantly coarser particles can remain dynamically coupled to the descending ash fingers, resulting in larger values of $d_{\max}$ whilst classical interpretations based on the assumption that particles are spherical would suggest limited instability development due to the absence of a fine, slow-settling, particle fraction (Manzella et al., 2015; Scollo et al., 2019; Fries et al., 2024). This extends the grain-size range participating in finger-driven sedimentation and suggests that finger formation does not necessarily require a substantial fraction of fine particles.

4.3 Ash fingers as the primary collective sedimentation mechanism in coarse-ash-dominated eruptions

Ash fingers have previously been suggested to promote ash-aggregation (Manzella et al., 2015; Scollo et al., 2017) . In these studies, turbulence generated by descending gravitational instabilities was proposed to enhance particle collision rates, thereby promoting aggregate formation. However, recent numerical simulations by Lemus et al., (2025) have questioned this interpretation, showing that turbulence generated inside ash fingers does not reach the intensity capable of affecting aggregation rates. The apparent association between ash fingers and aggregates in previous eruptions may instead arise because both processes are favoured in fine ash-rich clouds (Brown et al., 2012; Van Eaton and Wilson, 2013; Manzella et al., 2015; Diaz-Vecino et al., 2022) and, therefore, commonly occur simultaneously.

The 23 July 2024 Etna eruption provides a unique example in which well-developed ash fingers formed in the absence of aggregation. Optical microscopy of both drone and ground collected samples reveals predominantly individual particles with no evidence of ash clustering (Fig. 10). In addition, fine particles are scarce in both the TGSD (Fig. 8b) and drone-based PM measurements. Because fine ash is generally considered a prerequisite for efficient aggregation, these observations demonstrate that ash fingers can develop independently of aggregation processes in coarse-ash-dominated eruptions.

This distinction has important implications for understanding collective sedimentation in different eruptive styles. Mafic eruptions are commonly characterized by coarser grain-size distributions and generally exhibit less aggregation than silica-rich eruptions. For example, during the 2021–2022 Tajogaite eruption (La Palma), ash aggregation was observed primarily during rainy periods, when the presence of liquid water enhanced particle sticking, whereas little to no aggregation was reported during dry conditions (Bonadonna et al., 2023) . In contrast, silicic eruptions frequently produce abundant fine ash, which promotes aggregate formation and makes aggregation a dominant mechanism controlling collective sedimentation and fallout dynamics (Carey and Sigurdsson, 1982; Gilbert and Lane, 1994; Bonadonna et al., 2002a, 2011; Durant et al., 2009; Rose and Durant, 2011; Brown et al., 2012; Van Eaton et al., 2015; Diaz-Vecino et al., 2022; Gabellini et al., 2025).

The absence of aggregation during the 2024 Etna eruption therefore highlights the unique role of ash fingers in coarse-ash-dominated fallout. In such systems, ash fingers may represent the primary mechanism of collective sedimentation, capable of modifying local grain-size distributions and deposition patterns even when aggregation is negligible or absent. This suggests

https://doi.org/10.5194/egusphere-2026-4051
Preprint. Discussion started: 23 September 2026
© Author(s) 2026. CC BY 4.0 License.

that the relative importance of ash fingers and aggregation is strongly dependent on eruptive style and grain-size characteristics, with ash fingers likely playing a particularly important role in mafic explosive eruptions where fine ash is limited.

4.4 Influence of ash fingers on particle settling and deposition

Despite their transient nature, occurring only during discrete intervals of the eruption, ash fingers exert a measurable influence on both the spatial pattern and grain-size characteristics of the resulting deposit. In particular, the occurrence of ash fingers is associated with abundant fine particles (<125 µm) in proximal depositional areas relative to what would be expected from standard settling of a coarse-dominated eruption at Mt. Etna (Andronico et al., 2014; Amadio et al., 2024) .

Within the deposit, a distinct finer trend is observed in the proximal western area (Group G1 samples) (Fig. 8c), whose grain-size distributions are comparable to samples from the distal eastern area (Group G3) (Fig. 8e), with a mode between 0.5ϕ and 1ϕ (~700 – 500 µm). This pattern is counterintuitive, as proximal deposits are typically expected to be coarser due to the preferential settling of larger particles near the vent (Carey and Sparks, 1986; Bonadonna et al., 1998; Saxby et al., 2018; Eychenne and Engwell, 2022). However, direct observations from the video sequences show that ash fingers were descending and depositing precisely in the sector corresponding to Group G1 particularly above the sampling location L1 (Fig. 4c), providing direct field-based evidence linking finger dynamics to localized sedimentation patterns. Additionally, wind profiles reveal a change in the wind direction with altitude, with lower atmospheric levels characterized by a westward component, in contrast to the eastward dominant transport at higher altitudes (Fig. 4d). This vertical wind structure provides a mechanism for the lateral displacement of descending ash fingers, which are advected toward the western sector when reaching lower altitudes. Such vertical wind shear has been shown to significantly modify particle trajectories and produce complex deposition patterns (Bonadonna et al., 2005a; Poulidis et al., 2018). The correspondence between this low-level westward flow, which is observed in the bending of the ash fingers during their descent (Fig. 5d and Video S2 in the Zenodo repository), and the location of Group G1 supports the interpretation that finger-driven sedimentation preferentially contributed to the deposition in this sector.

This interpretation is further supported by the high mass fraction of particles below the calculated particle size threshold ($d_{\mathrm{max-ia}}$= 0.35ϕ or 785 µm) in these samples (Fig. 8a). Group G1 exhibits some of the highest proportions of particles smaller than $d_{\mathrm{max-ia}}$ with values reaching up to ~ 80% in sample C1 and exceeding ~30-60% across C2-C5. A similar temporal evolution is observed by the LPM measurements (Fig. 7), where the fraction of particles below $d_{\mathrm{max-ia}}$ increases markedly during the interval of ash finger occurrence, and approaches values close to 100% at peak activity (from 08:20 to 08:40 LT). However, relating the LPM signal directly to the observed ash fingers is not straightforward because sedimentation at the ground does not occur simultaneously with processes taking place within the volcanic cloud. First-order calculations, using the range of finger descent velocities (2.1 – 4.5 ms^{-1}), and wind speeds below the finger front (8.5 -11.9 m s^{-1}), suggest transport times of approximately 11-23 minutes and horizontal drift distances of approximately 5.5 – 16.4 km. These timescales are comparable to the delay between variation in MER and LPM grain-size signals. However, the finger velocity measurements represent some uncertainty due to the difficult visual conditions in the videos and their trajectories are unlikely to be purely

© Author(s) 2026. CC BY 4.0 License.

ballistics. Video observations show that fingers progressively bend (Fig. 5d) and lose coherence during descent and are observed directly above site L1 (Video S1 in the Zenodo repository), suggesting finger formation may occur continuously beneath the cloud. Nevertheless, it is evident from our results that finger affect proximal deposition, whilst most work predict that they only influence the sedimentation of fine volcanic ash in distal regions (Carazzo and Jellinek, 2012; Manzella et al., 2015).

4.5 Ash finger implementation in ash transport and dispersion models

TEPHRA2 provides a useful first-order framework for investigating the potential effects of ash finger settling on tephra deposition. By comparing baseline and finger-modified simulation within the same modelling framework, the relative influence of finger driven settling can be isolated without the additional complexity introduced by plume evolution, local meteorology and topographic effects. The simulations show only marginal differences in deposit mass loading between the finger and baseline scenarios, despite explicitly imposing enhanced settling velocities for particles below $d_{\mathrm{max-sa}}$. This limited sensitivity arises directly from the grain-size characteristics of the deposit, as the mass fraction of particles finer than $d_{\mathrm{max-sa}}$ is below 5 wt.% (Fig. 11c). Consequently, modifying the settling velocities of these particles produces only negligible changes in the predicted deposit mass loading. The similarity between the baseline and finger-modified isomass maps (Fig. 11a-b) therefore reflects not only a limitation of the ash-finger parameterization, but also a more fundamental limitation of the underlying modelling framework.

Specifically, the current implementation relies on the settling velocities predicted by TEPHRA2, which assumes spherical particle geometries. Volcanic ash particles, however, are highly irregular, and neglecting particle morphology systematically overestimates their terminal velocities (Wilson and Huang, 1979; Coltelli et al. 2008; Mele et al., 2011; Bagheri and Bonadonna, 2016a; Saxby et al., 2018, 2020). As a consequence, the maximum grain size susceptible to ash-finger entrainment under the spherical assumption ($d_{\mathrm{max-sa}}$) is substantially smaller than that obtained when particle shape is explicitly considered ($d_{\mathrm{max-ia}}$). This discrepancy is critical because it determines which portion of the grain-size distribution is assumed to participate in finger-driven sedimentation

Under the spherical assumption, only a very fine and volumetrically insignificant fraction of the deposit falls below $d_{\mathrm{max-sa}}$ (Fig. 11c). In contrast, the fraction of particles finer than $d_{\mathrm{max-ia}}$ is considerably larger (Fig. 8b), implying that ash fingers may influence a much broader portion of the grain-size distribution than currently represented by the model. The weak response observed in the finger-modified simulation is therefore not evidence that ash fingers have a negligible impact on tephra sedimentation, but rather that the spherical-particle framework identifies too small a fraction of particles as susceptible to finger entrainment. At the same time, incorporating $d_{\mathrm{max-ia}}$ directly into the current modelling framework is not straightforward. Doing so would require assigning enhanced sedimentation rates to a substantially larger and more mass-dominant fraction of the grain-size distribution. Because TEPHRA2 represents particle transport through independent settling trajectories, such an approach could produce non-physical behaviour, including unrealistic "rafting" of coarser particles

(Bagheri et al., 2016). This highlights a fundamental incompatibility between the physical processes associated with ash fingers and the assumptions underlying conventional advection-diffusion tephra dispersal models.

These findings have broader implications for volcanic ash forecasting and hazard assessment. Operational dispersal models are widely used to predict ash-cloud transport, ground accumulation, and associated impacts on infrastructure, aviation, and civil protection. If particle morphology is not adequately represented, the models may systematically misidentify the grain-size fraction susceptible to aggregation and ash-finger transport, leading to inaccurate predictions of sedimentation patterns and deposit mass loading. The present results therefore suggest that improving the representation of particle shape may be as important as improving the representation of aggregation and ash-finger processes themselves.

To our knowledge, this study represents the first attempt to incorporate field-constrained ash-finger dynamics into a tephra dispersal model. Although the modified TEPHRA2 framework is unable to reproduce the depositional signature inferred from field observations, the exercise provides an important quantitative benchmark. The persistent discrepancies between simulated and observed deposits, particularly the overestimation of proximal accumulation and the underestimation of distal deposition, indicate that the effects of ash fingers cannot be captured through a simple modification of settling velocity within a spherical-particle framework. However, these discrepancies likely also reflect the inability of the model to fully reproduce the complexity of the observed eruption dynamics. In particular, the observed plume exhibited asymmetry and local-scale motions, including backward transport (Fig. 5d) that may have influenced tephra deposition but are not represented in TEPHRA2. Future developments will likely require modelling approaches that explicitly account for particle morphology and the collective sedimentation processes associated with ash fingers and aggregation.

5 Conclusions

In this study, we combined deposit characterization from ground and drone-collected samples, thin-section analyses, LPM observations, and numerical simulations to investigate the physical controls on ash finger formation, their influence on proximal deposition, and the capacity of current dispersal models to reproduce their effects. The 23 July 2024, eruption offers a rare natural end-member case: a coarse-dominated deposit entirely free of ash aggregation, yet exhibiting well developed ash fingers. This combination allows us to isolate the specific influence of ash fingers on particle transport. Our results provide new constraints on the conditions required for finger development and highlight key limitations in existing modelling approaches. In particular:

- Ash fingers can form even in the absence of fine ash, demonstrating that fine particles are not a prerequisite for their formation during this eruption. This finding decouples finger formation from ash aggregation processes, as neither the deposit nor the airborne samples contain evidence of aggregates. This challenges the prevailing view that a relative abundance of fine material is a condition for finger development and that ash fingers and ash aggregation are intrinsically coupled.

https://doi.org/10.5194/egusphere-2026-4051
Preprint. Discussion started: 23 September 2026
© Author(s) 2026. CC BY 4.0 License.

- During the 23 July 2024 Etna event, ash fingers only occurred when MER > 2.5×10^5 kg s^{-1}, indicating that a minimum particle concentration is required even in coarse-ash dominated eruptions. These results are consistent with previous field observations linking ash finger occurrence to relatively high MER and extend them to eruptions lacking a significant fine ash component.
- By incorporating particle shape into settling velocity calculations, we refine the estimation of d_{max} and demonstrate that irregular particles of up to 950 µm can remain entrained within descending ash fingers. This widens the grain-size range affected by collective sedimentation and shows that finger-driven transport is not restricted to fine ash but can affect the settling behaviour of coarse particles.
- Although ash fingers are a transient phenomenon, they locally could modify deposition by increasing the proportion of coarse ash (710–500 µm) in proximal areas and modify the local grain-size distribution towards finer values. In the absence of a substantial fine-ash fraction (<63 µm), these effects do not generate a clear depositional signature such as bimodality. Nevertheless, the results indicate that ash fingers may be the primary process driving collective sedimentation in coarse-ash-dominated, silica-poor eruptions, where ash aggregation is largely suppressed by the scarcity of fine particles. This contrasts with silica-rich eruptions, where abundant fine ash promotes aggregation and collective settling through aggregate formation. As such, ash fingers should be considered a key mechanism controlling tephra sedimentation in mafic explosive eruptions.
- TEPHRA2 simulations show only minor differences between the finger-driven and individual-settling scenarios because the grain-size fraction below $d_{\mathrm{max-sa}}$, derived under the spherical-particle assumption, represents only a negligible proportion of the total deposit mass. This result highlights a fundamental limitation of conventional tephra-dispersal models; by neglecting particle morphology, they systematically misrepresent settling velocities and underestimate the grain-size range susceptible to ash-finger transport ($d_{\mathrm{max-ia}}$). Consequently, key depositional features associated with ash fingers, including the preferential transport and deposition of finer particles, cannot be reproduced within a standard advection–diffusion framework.
- This study represents the first field-constrained attempt to incorporate ash-finger dynamics into a tephra-dispersal model. While the current implementation does not fully reproduce the observed depositional signature of ash fingers, it provides an important quantitative benchmark and identifies particle shape as a critical control on ash-finger sedimentation. The results suggest that future forecasting and hazard-assessment models should move beyond the spherical-particle assumption and explicitly account for particle morphology and collective sedimentation processes in order to improve predictions of tephra transport, deposition, and associated volcanic hazards.

© Author(s) 2026. CC BY 4.0 License.

Code and data availability

The datasets generated and analysed during this study are publicly available through the following Zenodo repository: https://doi.org/10.5281/zenodo.21242583. The repository contains the raw datasets used in the analyses presented in this manuscript, including plume-height measurements, Mass Eruption Rate (MER) estimates, Optical Particle Counter (OPC) measurements, Laser Precipitation Monitor (LPM) measurements, grain-size distribution of the collected tephra samples, particle shape and density measurements, and videos of the volcanic plume showing ash fingers (Video S1 and S2). The modified TEPHRA2 code developed and used in this study is available from the corresponding author upon reasonable request.

Supplement link

The supplement related to this article is available online at [LINK]

Author contributions

CDV, AF, ST, RS, CB, and JL conceived and planned the field campaign with the local logistic support of SS. CDV, AF, ST, RS, JL, SS, FA, and LP conducted field and laboratory measurements. CDV, AF, ST, JL, Rs, and FA processed and analysed the data. VFL and AP provided support for modelling and code development. CDV drafted the manuscript under the supervision of CB. All authors reviewed, edited, and approved the final version of the manuscript.

Competing interests

The contact author has declared that none of the authors has any competing interests.

Disclaimer

Copernicus Publications adds a standard disclaimer: "Copernicus Publications remains neutral with regard to jurisdictional claims made in the text, published maps, institutional affiliations, or any other geographical representation in this paper. While Copernicus Publications makes every effort to include appropriate place names, the final responsibility lies with the authors. Views expressed in the text are those of the authors and do not necessarily reflect the views of the publisher."

Acknowledgements

Authors are grateful to Amanda Clarke, Jeremy Phillips and Paul Jarvis for their constructive discussions and valuable contributions to the interpretation of the deposit results. WRF simulations were performed on the HPC cluster Aether at the University of Bremen.

https://doi.org/10.5194/egusphere-2026-4051
Preprint. Discussion started: 23 September 2026
© Author(s) 2026. CC BY 4.0 License.

Financial support

790 The project was fully funded by the Swiss National Science Foundation grant #200020_204315\1.

F.A. was supported by a scholarship funded by Ministerial Decree No. 351 of 9.4.2022, under the PNRR—funded by the European Union—NextGenerationEU

Review statement

The review statement will be added by Copernicus Publications listing the handling editor as well as all contributing referees 795 according to their status anonymous or identified.

https://doi.org/10.5194/egusphere-2026-4051
Preprint. Discussion started: 23 September 2026
© Author(s) 2026. CC BY 4.0 License.

References

- Amadio, F., Pioli, L., and Scollo, S.: Constraining proximal grainsize distribution of tephra from paroxysmal eruptions at Etna volcano, Journal of Volcanology and Geothermal Research, 454, 108164, https://doi.org/10.1016/j.jvolgeores.2024.108164, 2024.
- Andronico, D., Scollo, S., Cristaldi, A., and Lo Castro, M. D.: Representivity of incompletely sampled fall deposits in estimating eruption source parameters: a test using the 12–13 January 2011 lava fountain deposit from Mt. Etna volcano, Italy, Bull Volcanol, 76, 861, https://doi.org/10.1007/s00445-014-0861-3, 2014.
- Andronico, D., Scollo, S., and Cristaldi, A.: Unexpected hazards from tephra fallouts at Mt Etna: The 23 November 2013 lava fountain, Journal of Volcanology and Geothermal Research, 304, 118–125, https://doi.org/10.1016/j.jvolgeores.2015.08.007, 2015.
- Andronico, D., Cannata, A., Di Grazia, G., and Ferrari, F.: The 1986–2021 paroxysmal episodes at the summit craters of Mt. Etna: Insights into volcano dynamics and hazard, Earth-Science Reviews, 220, 103686, https://doi.org/10.1016/j.earscirev.2021.103686, 2021.
- Bagheri, G. and Bonadonna, C.: Chapter 2 - Aerodynamics of Volcanic Particles: Characterization of Size, Shape, and Settling Velocity, in: Volcanic Ash, edited by: Mackie, S., Cashman, K., Ricketts, H., Rust, A., and Watson, M., Elsevier, 39–52, https://doi.org/10.1016/B978-0-08-100405-0.00005-7, 2016a.
- Bagheri, G. and Bonadonna, C.: On the drag of freely falling non-spherical particles, Powder Technology, 301, 526–544, https://doi.org/10.1016/j.powtec.2016.06.015, 2016b.
- Bagheri, G., Rossi, E., Biass, S., and Bonadonna, C.: Timing and nature of volcanic particle clusters based on field and numerical investigations, Journal of Volcanology and Geothermal Research, 327, 520–530, https://doi.org/10.1016/j.jvolgeores.2016.09.009, 2016.
- Beckett, F., Rossi, E., Devenish, B., Witham, C., and Bonadonna, C.: Modelling the size distribution of aggregated volcanic ash and implications for operational atmospheric dispersion modelling, Atmos. Chem. Phys., 22, 3409–3431, https://doi.org/10.5194/acp-22-3409-2022, 2022.
- Behncke, B., Branca, S., Corsaro, R. A., De Beni, E., Miraglia, L., and Proietti, C.: The 2011–2012 summit activity of Mount Etna: Birth, growth and products of the new SE crater, Journal of Volcanology and Geothermal Research, 270, 10–21, https://doi.org/10.1016/j.jvolgeores.2013.11.012, 2014.
- Biass, S., Scaini, C., Bonadonna, C., Folch, A., Smith, K., and Höskuldsson, A.: A multi-scale risk assessment for tephra fallout and airborne concentration from multiple Icelandic volcanoes – Part 1: Hazard assessment, Natural Hazards and Earth System Sciences, 14, 2265–2287, https://doi.org/10.5194/nhess-14-2265-2014, 2014.
- Bonadonna, C. and Costa, A.: Estimating the volume of tephra deposits: A new simple strategy, Geology, 40, 415–418, https://doi.org/10.1130/G32769.1, 2012.

- Bonadonna, C. and Houghton, B. F.: Total grain-size distribution and volume of tephra-fall deposits, Bull Volcanol, 67, 441–456, https://doi.org/10.1007/s00445-004-0386-2, 2005.
- Bonadonna, C., Ernst, G. G. J., and Sparks, R. S. J.: Thickness variations and volume estimates of tephra fall deposits: the importance of particle Reynolds number, Journal of Volcanology and Geothermal Research, 81, 173–187, https://doi.org/10.1016/S0377-0273(98)00007-9, 1998.
- Bonadonna, C., Macedonio, G., and Sparks, R. S. J.: Numerical modelling of tephra fallout associated with dome collapses and Vulcanian explosions: application to hazard assessment on Montserrat, Geological Society, London, Memoirs, 21, 517–537, https://doi.org/10.1144/GSL.MEM.2002.021.01.23, 2002a.
- Bonadonna, C., Calder, E. S., Sparks, R. S. J., Lejeune, A. M., Mayberry, G. C., Rose, W. I., Choux, C., Jackson, P., Young, S. R., Loughlin, S. C., Norton, G. E., and Ryan, G.: Tephra fallout in the eruption of Soufrière Hills Volcano, Montserrat, Geological Society Memoir, 21, 483–516, https://doi.org/10.1144/GSL.MEM.2002.021.01.22, 2002b.
- Bonadonna, C., Phillips, J. C., and Houghton, B. F.: Modeling tephra sedimentation from a Ruapehu weak plume eruption, Journal of Geophysical Research: Solid Earth, 110, https://doi.org/10.1029/2004JB003515, 2005a.
- Bonadonna, C., Connor, C. B., Houghton, B. F., Connor, L., Byrne, M., Laing, A., and Hincks, T. K.: Probabilistic modeling of tephra dispersal: Hazard assessment of a multiphase rhyolitic eruption at Tarawera, New Zealand, Journal of Geophysical Research: Solid Earth, 110, https://doi.org/10.1029/2003JB002896, 2005b.
- Bonadonna, C., Connor, L., Connor, C. B., and Courtland, L. M.: Tephra2, 2010.
- Bonadonna, C., Genco, R., Gouhier, M., Pistolesi, M., Cioni, R., Alfano, F., Hoskuldsson, A., and Ripepe, M.: Tephra sedimentation during the 2010 Eyjafjallajökull eruption (Iceland) from deposit, radar, and satellite observations, Journal of Geophysical Research: Solid Earth, 116, https://doi.org/10.1029/2011JB008462, 2011.
- Bonadonna, C., Pistolesi, M., Dominguez, L., Freret-Lorgeril, V., Rossi, E., Fries, A., Biass, S., Voloschina, M., Lemus, J., Romero, J. E., Zanon, V., Pastore, C., Reyes Hardy, M.-P., Di Maio, L. S., Gabellini, P., Martin-Lorenzo, A., Rodriguez, F., and Perez, N. M.: Tephra sedimentation and grainsize associated with pulsatory activity: the 2021 Tajogaite eruption of Cumbre Vieja (La Palma, Canary Islands, Spain), Front. Earth Sci., 11, https://doi.org/10.3389/feart.2023.1166073, 2023.
- Branca, S. and Carlo, P. D.: Types of eruptions of Etna volcano AD 1670–2003: implications for short-term eruptive behaviour, Bull Volcanol, 67, 732–742, https://doi.org/10.1007/s00445-005-0412-z, 2005.
- Brandt, L. and Coletti, F.: Particle-Laden Turbulence: Progress and Perspectives, Annu. Rev. Fluid Mech., 54, 159–189, https://doi.org/10.1146/annurev-fluid-030121-021103, 2022.
- Brown, R. J., Bonadonna, C., and Durant, A. J.: A review of volcanic ash aggregation, Physics and Chemistry of the Earth, Parts A/B/C, 45–46, 65–78, https://doi.org/10.1016/j.pce.2011.11.001, 2012.
- Calvari, S. and Nunnari, G.: Reawakening of Voragine, the Oldest of Etna's Summit Craters: Insights from a Recurrent Episodic Eruptive Behavior, Remote Sensing, 16, 4278, https://doi.org/10.3390/rs16224278, 2024.

- Calvari, S., Cannavò, F., Bonaccorso, A., Spampinato, L., and Pellegrino, A. G.: Paroxysmal Explosions, Lava Fountains and Ash Plumes at Etna Volcano: Eruptive Processes and Hazard Implications, Front. Earth Sci., 6, https://doi.org/10.3389/feart.2018.00107, 2018.
- Carazzo, G. and Jellinek, A. M.: A new view of the dynamics, stability and longevity of volcanic clouds, Earth and Planetary Science Letters, 325–326, 39–51, https://doi.org/10.1016/j.epsl.2012.01.025, 2012.
- Carey, S.: Influence of convective sedimentation on the formation of widespread tephra fall layers in the deep sea, Geol, 25, 839, https://doi.org/10.1130/0091-7613(1997)025%3C0839:IOCSOT%3E2.3.CO;2, 1997.
- Carey, S. and Sparks, R. S. J.: Quantitative models of the fallout and dispersal of tephra from volcanic eruption columns, Bull Volcanol, 48, 109–125, https://doi.org/10.1007/BF01046546, 1986.
- Carey, S. N. and Sigurdsson, H.: Influence of particle aggregation on deposition of distal tephra from the May 18, 1980, eruption of Mount St. Helens volcano, Journal of Geophysical Research: Solid Earth, 87, 7061–7072, 1982.
- Coltelli, M., Miraglia, L., and Scollo, S.: Characterization of shape and terminal velocity of tephra particles erupted during the 2002 eruption of Etna volcano, Italy, Bull Volcanol, 70, 1103–1112, https://doi.org/10.1007/s00445-007-0192-8, 2008.
- Connor, L. J. and Connor, C. B.: Inversion is the key to dispersion: understanding eruption dynamics by inverting tephra fallout, in: Statistics in Volcanology, vol. 1, edited by: Mader, H. M., Coles, S. G., Connor, C. B., and Connor, L. J., Geological Society of London, 0, https://doi.org/10.1144/IAVCEI001.18, 2006.
- Corsaro, R. A., Andronico, D., Behncke, B., Branca, S., Caltabiano, T., Ciancitto, F., Cristaldi, A., De Beni, E., La Spina, A., Lodato, L., Miraglia, L., Neri, M., Salerno, G., Scollo, S., and Spata, G.: Monitoring the December 2015 summit eruptions of Mt. Etna (Italy): Implications on eruptive dynamics, Journal of Volcanology and Geothermal Research, 341, 53–69, https://doi.org/10.1016/j.jvolgeores.2017.04.018, 2017.
- Degruyter, W. and Bonadonna, C.: Improving on mass flow rate estimates of volcanic eruptions, Geophysical Research Letters, 39, https://doi.org/10.1029/2012GL052566, 2012.
- Diaz-Vecino, M. C., Rossi, E., Freret-Lorgeril, V., Fries, A., Gabellini, P., Lemus, J., Pollastri, S., Poulidis, A. P., Iguchi, M., and Bonadonna, C.: Aerodynamic characteristics and genesis of aggregates at Sakurajima Volcano, Japan, Sci Rep, 12, 2044, https://doi.org/10.1038/s41598-022-05854-z, 2022.
- Durant, A. J.: RESEARCH FOCUS: Toward a realistic formulation of fine-ash lifetime in volcanic clouds, Geology, 43, 271–272, https://doi.org/10.1130/focus032015.1, 2015.
- Durant, A. J., Rose, W. I., Sarna-Wojcicki, A. M., Carey, S., and Volentik, A. C. M.: Hydrometeor-enhanced tephra sedimentation: Constraints from the 18 May 1980 eruption of Mount St. Helens, J. Geophys. Res., 114, 2008JB005756, https://doi.org/10.1029/2008JB005756, 2009.
- Egan, S. D., Stuefer, M., Webley, P. W., Lopez, T., Cahill, C. F., and Hirtl, M.: Modeling volcanic ash aggregation processes and related impacts on the April–May 2010 eruptions of Eyjafjallajökull volcano with WRF-Chem, Natural Hazards and Earth System Sciences, 20, 2721–2737, https://doi.org/10.5194/nhess-20-2721-2020, 2020.

https://doi.org/10.5194/egusphere-2026-4051
Preprint. Discussion started: 23 September 2026
© Author(s) 2026. CC BY 4.0 License.

- Eliasson, J., Yoshitani, J., Weber, K., Yasuda, N., Iguchi, M., and Vogel, A.: Airborne Measurement in the Ash Plume from Mount Sakurajima: Analysis of Gravitational Effects on Dispersion and Fallout, International Journal of Atmospheric Sciences, 2014, 1–16, https://doi.org/10.1155/2014/372135, 2014.
- Eychenne, J. and Engwell, S. L.: The grainsize of volcanic fall deposits: Spatial trends and physical controls, GSA Bulletin, https://doi.org/10.1130/B36275.1, 2022.
- Eychenne, J. and Le Pennec, J.-L.: Sigmoidal particle density distribution in a subplinian scoria fall deposit, Bull Volcanol, 74, 2243–2249, https://doi.org/10.1007/s00445-012-0671-4, 2012.
- Fierstein, J. and Nathenson, M.: Another look at the calculation of fallout tephra volumes, Bull Volcanol, 54, 156–167, https://doi.org/10.1007/BF00278005, 1992.
- Folch, A., Costa, A., and Macedonio, G.: FALL3D: A computational model for transport and deposition of volcanic ash, Computers & Geosciences, 35, 1334–1342, https://doi.org/10.1016/j.cageo.2008.08.008, 2009.
- Folch, A., Costa, A., Durant, A., and Macedonio, G.: A model for wet aggregation of ash particles in volcanic plumes and clouds: 2. Model application, Journal of Geophysical Research: Solid Earth, 115, https://doi.org/10.1029/2009JB007176, 2010.
- Freret-Lorgeril, V., Donnadieu, F., Eychenne, J., Soriaux, C., and Latchimy, T.: In situ terminal settling velocity measurements at Stromboli volcano: Input from physical characterization of ash, Journal of Volcanology and Geothermal Research, 374, 62–79, https://doi.org/10.1016/j.jvolgeores.2019.02.005, 2019.
- Freret-Lorgeril, V., Gilchrist, J., Donnadieu, F., Jellinek, A. M., Delanoë, J., Latchimy, T., Vinson, J. P., Caudoux, C., Peyrin, F., Hervier, C., and Valade, S.: Ash sedimentation by fingering and sediment thermals from wind-affected volcanic plumes, Earth and Planetary Science Letters, 534, 116072, https://doi.org/10.1016/j.epsl.2020.116072, 2020.
- Freret-Lorgeril, V., Bonadonna, C., Rossi, E., Poulidis, A. P., and Iguchi, M.: New insights into real-time detection of tephra grainsize, settling velocity and sedimentation rate, Sci Rep, 12, 4650, https://doi.org/10.1038/s41598-022-08711-1, 2022.
- Fries, A., Lemus, J., Jarvis, P. A., Clarke, A. B., Phillips, J. C., Manzella, I., and Bonadonna, C.: The Influence of Particle Concentration on the Formation of Settling-Driven Gravitational Instabilities at the Base of Volcanic Clouds, Front. Earth Sci., 9, 640090, https://doi.org/10.3389/feart.2021.640090, 2021.
- Fries, A., Lemus, J., Jarvis, P. A., Clarke, A. B., Phillips, J. C., Manzella, I., and Bonadonna, C.: Particle Concentrations and Sizes for the Onset of Settling-Driven Gravitational Instabilities: Experimental Validation and Application to Volcanic Ash Clouds, Journal of Geophysical Research: Solid Earth, 129, e2024JB029117, https://doi.org/10.1029/2024JB029117, 2024.
- Fries, A. A.: Field and experimental characterisation of tephra sedimentation and resuspension processes, Université de Genève, https://doi.org/10.13097/ARCHIVE-OUVERTE/UNIGE:163115, 2022.

- Gabellini, P., Rossi, E., Cioni, R., Pistolesi, M., Baumgartner, L. P., and Bonadonna, C.: X-Ray micro-tomography unveils the internal features of volcanic ash aggregates, Commun Earth Environ, 6, 521, https://doi.org/10.1038/s43247-025-02378-y, 2025.
- Ganser, G. H.: A rational approach to drag prediction of spherical and nonspherical particles, Powder Technology, 77, 143–152, https://doi.org/10.1016/0032-5910(93)80051-B, 1993.
- Gilbert, J. S. and Lane, S. J.: The origin of accretionary lapilli, Bull Volcanol, 56, 398–411, https://doi.org/10.1007/BF00326465, 1994.
- Gilchrist, J. T. and Jellinek, A. M.: Sediment waves and the gravitational stability of volcanic jets, Bull Volcanol, 83, 64, https://doi.org/10.1007/s00445-021-01472-1, 2021.
- Giuffrida, M., Cardone, M., Zuccarello, F., and Viccaro, M.: Etna 2011–2022: Discoveries from a decade of activity at the volcano, Earth-Science Reviews, 245, 104563, https://doi.org/10.1016/j.earscirev.2023.104563, 2023.
- Hoyal, D. C. J. D., Bursik, M. I., and Atkinson, J. F.: Settling-driven convection: A mechanism of sedimentation from stratified fluids, J. Geophys. Res., 104, 7953–7966, https://doi.org/10.1029/1998JC900065, 1999.
- INGV (Istituto Nazionale di Geofisica e Vulcanologia): *Etna – Bollettino Settimanale, settimana di riferimento 22/07/2024–28/07/2024 (Rep. N. 31/2024 ETNA)*, issued 30 July 2024.
- Inman, D. L.: Measures for describing the size distribution of sediments, Journal of Sedimentary Research, 22, 125–145, 1952.
- Jacobs, C. T., Goldin, T. J., Collins, G. S., Piggott, M. D., Kramer, S. C., Melosh, H. J., Wilson, C. R. G., and Allison, P. A.: An improved quantitative measure of the tendency for volcanic ash plumes to form in water: implications for the deposition of marine ash beds, Journal of Volcanology and Geothermal Research, 290, 114–124, https://doi.org/10.1016/j.jvolgeores.2014.10.015, 2015.
- Lemus, J.: Modelling Settling-Driven Gravitational Instabilities at the base of volcanic clouds, Université de Genève, https://doi.org/10.13097/ARCHIVE-OUVERTE/UNIGE:162742, 2022.
- Lemus, J., Rossi, E., Fries, A., Latt, J., and Bonadonna, C.: Particle Aggregation and Settling-Driven Gravitational Instabilities: A Combined Impact on Volcanic Ash Sedimentation, Journal of Geophysical Research: Solid Earth, 130, e2024JB030855, https://doi.org/10.1029/2024JB030855, 2025.
- Manzella, I., Bonadonna, C., Phillips, J. C., and Monnard, H.: The role of gravitational instabilities in deposition of volcanic ash, Geology, 43, 211–214, https://doi.org/10.1130/G36252.1, 2015.
- Mele, D., Dellino, P., Sulpizio, R., and Braia, G.: A systematic investigation on the aerodynamics of ash particles, Journal of Volcanology and Geothermal Research, 203, 1–11, https://doi.org/10.1016/j.jvolgeores.2011.04.004, 2011.
- Penlou, B., Roche, O., Manga, M., and van den Wildenberg, S.: Experimental Measurement of Enhanced and Hindered Particle Settling in Turbulent Gas-Particle Suspensions, and Geophysical Implications, Journal of Geophysical Research: Solid Earth, 128, e2022JB025809, https://doi.org/10.1029/2022JB025809, 2023.

- Poulidis, A. P., Phillips, J. C., Renfrew, I. A., Barclay, J., Hogg, A., Jenkins, S. F., Robertson, R., and Pyle, D. M.: Meteorological Controls on Local and Regional Volcanic Ash Dispersal, Sci Rep, 8, 6873, https://doi.org/10.1038/s41598-018-24651-1, 2018.
- Pyle, D. M.: The thickness, volume and grainsize of tephra fall deposits, Bull Volcanol, 51, 1–15, https://doi.org/10.1007/BF01086757, 1989.
- Rose, W. I. and Durant, A. J.: Fate of volcanic ash: Aggregation and fallout, Geology, 39, 895–896, https://doi.org/10.1130/focus092011.1, 2011.
- Saxby, J., Beckett, F., Cashman, K., Rust, A., and Tennant, E.: The impact of particle shape on fall velocity: Implications for volcanic ash dispersion modelling, Journal of Volcanology and Geothermal Research, 362, 32–48, https://doi.org/10.1016/j.jvolgeores.2018.08.006, 2018.
- Saxby, J., Rust, A., Beckett, F., Cashman, K., and Rodger, H.: Estimating the 3D shape of volcanic ash to better understand sedimentation processes and improve atmospheric dispersion modelling, Earth and Planetary Science Letters, 534, 116075, https://doi.org/10.1016/j.epsl.2020.116075, 2020.
- Schultz, D. M., Kanak, K. M., Straka, J. M., Trapp, R. J., Gordon, B. A., Zrnić, D. S., Bryan, G. H., Durant, A. J., Garrett, T. J., Klein, P. M., and Lilly, D. K.: The Mysteries of Mammatus Clouds: Observations and Formation Mechanisms, Journal of the Atmospheric Sciences, 63, 2409–2435, https://doi.org/10.1175/JAS3758.1, 2006.
- Schwaiger, H. F., Denlinger, R. P., and Mastin, L. G.: Ash3d: A finite-volume, conservative numerical model for ash transport and tephra deposition, https://doi.org/10.1029/2011JB008968, 2012.
- Scollo, S., Prestifilippo, M., Spata, G., D'Agostino, M., and Coltelli, M.: Monitoring and forecasting Etna volcanic plumes, Natural Hazards and Earth System Sciences, 9, 1573–1585, https://doi.org/10.5194/nhess-9-1573-2009, 2009.
- Scollo, S., Bonadonna, C., and Manzella, I.: Settling-driven gravitational instabilities associated with volcanic clouds: new insights from experimental investigations, Bull Volcanol, 79, 39, https://doi.org/10.1007/s00445-017-1124-x, 2017.
- Scollo, S., Prestifilippo, M., Bonadonna, C., Cioni, R., Corradini, S., Degruyter, W., Rossi, E., Silvestri, M., Biale, E., Carparelli, G., Cassisi, C., Merucci, L., Musacchio, M., and Pecora, E.: Near-Real-Time Tephra Fallout Assessment at Mt. Etna, Italy, Remote Sensing, 11, 2987, https://doi.org/10.3390/rs11242987, 2019.
- Simionato, R., Jarvis, P. A., Rossi, E., and Bonadonna, C.: PlumeTraP: A New MATLAB-Based Algorithm to Detect and Parametrize Volcanic Plumes from Visible-Wavelength Images, Remote Sensing, 14, 1766, https://doi.org/10.3390/rs14071766, 2022.
- Simionato, R., Jarvis, P. A., Rossi, E., Fries, A., Pistolesi, M., Aguilar, R., and Bonadonna, C.: Combining Visible- and Infrared-Wavelength Observations With Numerical Modeling to Describe Vulcanian Eruption Plumes at Sabancaya, Peru, Journal of Geophysical Research: Solid Earth, 129, e2024JB029326, https://doi.org/10.1029/2024JB029326, 2024.
- Skamarock, W. C., Klemp, J. B., Dudhia, J., Gill, D. O., Liu, Z., Berner, J., Wang, W., Powers, J. G., Duda, M. G., Barker, D. M., and others: A description of the advanced research WRF version 4, NCAR tech. note ncar/tn-556+ str, 145, 2019.

- Snee, E., Jarvis, P. A., Simionato, R., Scollo, S., Prestifilippo, M., Degruyter, W., and Bonadonna, C.: Image analysis of volcanic plumes: A simple calibration tool to correct for the effect of wind, Volcanica, 6, 447–458, https://doi.org/10.30909/vol.06.02.447458, 2023.
- Soci, C., Hersbach, H., Simmons, A., Poli, P., Bell, B., Berrisford, P., Horányi, A., Muñoz-Sabater, J., Nicolas, J., Radu, R., Schepers, D., Villaume, S., Haimberger, L., Woollen, J., Buontempo, C., and Thépaut, J.-N.: The ERA5 global reanalysis from 1940 to 2022, Quarterly Journal of the Royal Meteorological Society, 150, 4014–4048, https://doi.org/10.1002/qj.4803, 2024.
- Takishita, K., Poulidis, A.-P., and Iguchi, M.: Tephra segregation profiles based on disdrometer observations and tephra dispersal modeling: Vulcanian eruptions of Sakurajima volcano, Japan, Earth Planets Space, 76, 29, https://doi.org/10.1186/s40623-023-01952-y, 2024.
- Thivet, S., Bagheri, G., Kornatowski, P. M., Fries, A., Lemus, J., Simionato, R., Díaz-Vecino, C., Rossi, E., Yamada, T., Scollo, S., and Bonadonna, C.: In situ volcanic ash sampling and aerosol–gas analysis based on UAS technologies (AeroVolc), Atmospheric Measurement Techniques, 18, 2803–2824, https://doi.org/10.5194/amt-18-2803-2025, 2025.
- Thivet, S., Simionato, R., Fries, A., Díaz-Vecino, C., Lemus, J., Fréret-Lorgeril, V., Poulidis, A. P., Iguchi, M., and Bonadonna, C.: In-situ evidence of volcanic ash aggregation during fallout from combined ground- and UAS-based observations, Sci Rep, 16, 15083, https://doi.org/10.1038/s41598-026-45460-x, 2026.
- Thomaidis, K., Troll, V. R., Deegan, F. M., Freda, C., Corsaro, R. A., Behncke, B., and Rafailidis, S.: A message from the ‘underground forge of the gods’: history and current eruptions at Mt Etna, Geology Today, 37, 141–149, https://doi.org/10.1111/gto.12362, 2021.
- Van Eaton, A. R. and Wilson, C. J. N.: The nature, origins and distribution of ash aggregates in a large-scale wet eruption deposit: Oruanui, New Zealand, Journal of Volcanology and Geothermal Research, 250, 129–154, https://doi.org/10.1016/j.jvolgeores.2012.10.016, 2013.
- Van Eaton, A. R., Mastin, L. G., Herzog, M., Schwaiger, H. F., Schneider, D. J., Wallace, K. L., and Clarke, A. B.: Hail formation triggers rapid ash aggregation in volcanic plumes, Nat Commun, 6, 7860, https://doi.org/10.1038/ncomms8860, 2015.
- Watt, S. F. L., Gilbert, J. S., Folch, A., Phillips, J. C., and Cai, X. M.: An example of enhanced tephra deposition driven by topographically induced atmospheric turbulence, Bull Volcanol, 77, 35, https://doi.org/10.1007/s00445-015-0927-x, 2015.
- Wilson, L. and Huang, T. C.: The influence of shape on the atmospheric settling velocity of volcanic ash particles, Earth and Planetary Science Letters, https://doi.org/10.1016/0012-821X(79)90179-1, 1979.
- Woods, A. W.: The fluid dynamics and thermodynamics of eruption columns, Bull Volcanol, 50, 169–193, https://doi.org/10.1007/BF01079681, 1988.